# Simulating quasi-static crack propagation by coupled peridynamics least square minimization with finite element method

**4 authors**, including:

Qibang Liu
Kansas State University
**4** PUBLICATIONS   **2** CITATIONS

Youqi Wang
Kansas State University
**38** PUBLICATIONS   **1,141** CITATIONS

# Simulating quasi-static crack propagation by coupled peridynamics least square minimization with finite element method

Qibang Liu[a,*], X.J. Xin[a], Jeff Ma[b] and Youqi Wang[a]

[a]*Department of Mechanical and Nuclear Engineering, Kansas State University, Manhattan, KS 66506, USA*
[b]*Parks College of Engineering, Aviation, and Technology, Saint Louis University, MO 63103,USA*

ARTICLE INFO

ABSTRACT

In this work, we present an innovative simulation method for quasi-static crack propagation in mixed-mode, within a new framework of coupled peridynamics least square minimization and finite element method (PDLSM-FEM). As the inertia effect is neglected for quasi-static problems, the governing equations for PDLSM-FEM can be solved implicitly without iterations. Displacements and stresses from PDLSM-FEM are used to compute the interaction integral, an extended version of the *J*-integral. The stress intensity factors (SIFs) are derived from the interaction integral and used in the maximum circumferential tensile stress failure criterion to predict the onset of crack propagation and the direction of propagation. New contributions in this work include the following: (1) developing a new framework for coupling PDLSM and FEM; (2) pioneering a quasi-static method for simulating crack propagation in peridynamics; (3) developing an element-based approach for selecting the interaction integral contour; and (4) proposing and implementing an innovative method for handling peridynamic bond breakage and crack growth. Quasi-static crack propagation simulation in this work provides a computationally efficient way to find the shape of the crack, and the current PDLSM-FEM model is straightforward and can be easily introduced into commercial finite element codes. Three numerical examples are carried out, and the results show that the proposed method evaluates SIFs accurately and captures crack growth as expected.

## 1. Introduction

Many problems of fundamental importance in solid mechanics involve pre-existing and propagating discontinuities such as cracks. As classical continuum theory employs spatial derivatives in its formulation and assumes the material is continuous as it deforms, it is inherently difficult to predict discontinuous behaviors such as failure of materials and structures. In light of the inadequacies of the classical continuum theory, Peridynamics (PD), which is based on non-local interactions and employs spatial integrals, was first introduced by Silling (2000). PD theory is better suited for failure analysis of materials and structures because its governing equations are defined by integral equations and remain valid at fracture surfaces.

PD theory has been extended from bond-based theory (Silling, 2000), which has a restriction of a fixed Poisson's ratio of 1/4 (Gerstle et al., 2005; Madenci and Oterkus, 2014; Bobaru et al., 2016), to the state-based one (Silling et al., 2007), which has no restriction on the value of Poisson's ratio. To date, both the bond-based and state-based PD theories have been successfully applied to various discontinuous problems, such as ice craters by impact (Song et al., 2019), the interaction between sea ice and wide vertical structures (Jia et al., 2019), dynamic response of ceramics tiles under impact loading (Chu et al., 2020). In all of the works quoted above, both bond-based and state-based PD theories were derived by equating the classical strain energy at a material point to that of PD with a complete circle or sphere interaction domain (Madenci and Oterkus, 2014). These formulas in PD theory, however, are not valid for a point located near a surface because its interaction domain is not a complete circle or sphere (Le and Bobaru, 2018). Furthermore, most published work on PD to date employs a simple meshless method with a one-point quadrature for cells. Such one-point quadrature requires a volume correction procedure to improve integration accuracy (Seleson, 2014). To remove these two drawbacks, Madenci et al. (2019) proposed a PD least squares minimization (PDLSM), and Liu and Xin (2021) proposed a revised non-ordinary state-based PD (RNOSBPD). Both methods were derived

---

*Corresponding author.
Email address:* qibangliu@ksu.edu. (Q. Liu)

by Taylor series expansion and the concept of non-local interactions of PD. Comparing to the finite element method (FEM), PD is computationally expensive. Thus, techniques for coupling PD with FEM were proposed to take advantage of these two methods, such as overlapping regions (Kilic and Madenci, 2010b), morphing strategy (Lubineau et al., 2012), fictitious nodes (Zaccariotto et al., 2017), splice method (Zaccariotto et al., 2018), adaptive coupling approach (Wang et al., 2019), and weighted residual method (Liu and Xin, 2021). Besides, some other techniques, such as dual-horizon PD model (Ren et al., 2017) and multi-horizon PD model (Jenabidehkordi and Rabczuk, 2019) were also proposed to improve the computational efficiency of PD.

PD theory describes damages by irreversible breakage of a bond, which is the non-local interaction of two material points. Thus, an appropriate failure criterion is very important to determine bond breakage in failure analysis by PD. The first failure criterion called critical stretch criterion is based on bond stretch (Silling and Askari, 2005) and the critical stretch value is derived by the interaction formulas of bond-based PD. Recently, Zhang and Qiao (2018) proposed a model for the calculation of the critical stretch in ordinary state-based PD (OSBPD). Based on the energy density stored in a deformed bond, the critical energy density criterion was proposed by Foster et al. (2011) and later was applied to plastic deformation by Madenci and Oterkus (2016). Zhang and Qiao (2019) discussed the limitations of the critical stretch and energy density criteria for pure mode $II$ or mode $II$ dominant fracture analysis and proposed a criterion named critical skew for quantitative OSBPD analysis of mode $II$ fracture. Since non-ordinary state-based PD (NOSBPD) recovers the concept of non-local stress and strain, an equivalent strain criterion (Warren et al., 2009) and a maximum principal stress criterion (Madenci et al., 2018) were employed to perform failure analysis by NOSBPD. However, the criterion that is based on stress and strain may depend strongly on mesh size, as the stress and strain fields near the crack tip exhibit singular behavior.

In general, PD is computationally expensive due to a large number of non-local interactions, much-refined mesh, and PD-based codes written in terms of dynamic equilibrium even for static problems. Typically, static problems in PD are solved by adopting an explicit dynamic relaxation method (Kilic and Madenci, 2010a) that determines steady-state solutions for a dynamic system by introducing fictitious mass and damping matrices. The explicit dynamic relaxation method is commonly preferred because it does not require large-matrix operations. Although implicit method requires matrix inversion, the stiffness matrix of a FEM model is symmetric and sparse and its inversion is relatively easier and fast computationally. In comparison, mesh refinement in PD increases the size of the stiffness matrix $\mathbf{K}$ and a large number of non-local interactions leads to a denser $\mathbf{K}$, both of which significantly increase the computational cost to solve for $\mathbf{K}^{-1}$. Coupling PD with FEM makes it easier to employ the implicit method to solve fracture problems since FEM nodes interact only with nodes in the same element and neighboring elements, making the number of interactions much smaller than that of a full PD model. Furthermore, FEM enables a much coarser mesh at regions far from the crack tips. Comparing to the explicit method, the implicit method of coupled PD with FEM does not need a large number of iterations for solution, and equilibrium is guaranteed if convergence is reached, thus it is more efficient for static problems (Ni et al., 2019).

In this work, we propose a new framework for coupling peridynamics least square minimization with finite element method (PDLSM-FEM) based on the weighted residual method, and conduct PDLSM-FEM simulations for quasi-static crack propagation under mixed-mode loading. As the inertia effects is neglected in quasi-static simulation, the current model provides an efficient way to find the shape of the crack. The PDLSM-FEM is straightforward and can be easily introduced into commercial finite element codes. A numerical method for the interaction integral ($I$-integral), an extended version of the $J$-integral, to calculate the stress intensity factors (SIFs) is proposed and implemented. Failure is based on the criterion of maximum circumferential tensile stress (Erdogan and Sih, 1963). The crack growth direction $\theta_c$ are determined by maximizing the circumferential tensile stress with respect to the orientation, and crack propagation is triggered when the equivalent SIF $K_{eq}$ of mixed-mode loading reaches the critical value of material fracture toughness $K_{Ic}$. As the $J$-integral is path independent, the proposed method is much more reliable and accurate than using near-tip stresses directly from the PD model which are sensitive to mesh refinement and less accurate. New contributions in this work include the following: (1) developing a new framework for coupling PDLSM and FEM; (2) pioneering a quasi-static method for simulating crack propagation in peridynamics; (3) developing an element-based approach for selecting the interaction integral contour; and (4) proposing and implementing an innovative method for handling peridynamic bond breakage and crack growth.

The remainder of this paper is outlined as follows. First, the theory of PDLSM is reviewed in Section 2. A new technique for coupling PDLSM with FEM based on the weighted residual method is developed and presented in Section 3, with more details presented in Appendix A. Next, the quasi-static crack growth simulation model for mixed-mode loading is proposed in Section 4. Three applications are performed to validate the proposed simulation

model in Section 5. Finally, concluding remarks are summarized in Section 6.

## 2. Peridynamics least square minimization (PDLSM)

In this section, the peridynamics least square Minimization (PDLSM) first developed by Madenci et al. (2019) is briefly reviewed for completeness. PDLSM employs the concept of PD interactions and LSM in conjunction with the Taylor series expansion. More detailed formulas essential for understanding PDLSM can be found in (Madenci et al., 2019).

In PD, the equation of motion is given by

$$\rho\ddot{\mathbf{u}} = \mathbf{L}(\mathbf{x}, t) + \mathbf{b}(\mathbf{x}, t), \tag{1}$$

where $\rho$ is the mass density, $\ddot{\mathbf{u}}$ is the acceleration, $\mathbf{b}$ is the external force vector, and $\mathbf{L}$ is the internal force vector. The internal force at point $\mathbf{x}$ is evaluated by the integration of bond force between points $\mathbf{x}$ and $\mathbf{x}'$ over the interaction domain $H_x$ of point $\mathbf{x}$, as shown in Fig. 1. Note that the interaction domain $H_x$ can be of a arbitrary shape, and not required to be a spherical or circle.
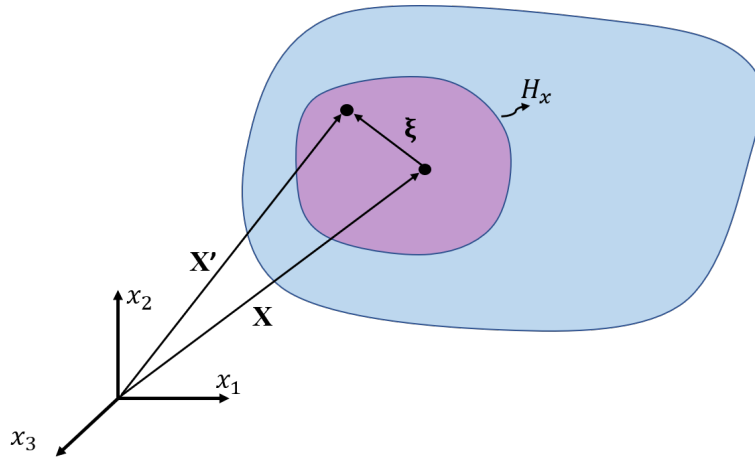


**Fig. 1:** Bond between point $\mathbf{x}'$ and $\mathbf{x}$ in the interaction domain $H_x$.

For a linear isotropic material response, the non-local internal force vector can be expressed as

$$\mathbf{L}^{pd} = \int_{H_x} \omega(|\boldsymbol{\xi}|)\mathbf{G}\boldsymbol{\eta}dV_{x'}, \tag{2}$$

and the non-local displacement gradient is

$$\nabla\mathbf{u}^{pd} = \int_{H_x} \omega(|\boldsymbol{\xi}|)\boldsymbol{\eta} \otimes \mathbf{g}dV_{x'}, \tag{3}$$

where $\boldsymbol{\xi} = \mathbf{x}' - \mathbf{x}$ and $\boldsymbol{\eta} = \mathbf{u}(\mathbf{x}') - \mathbf{u}(\mathbf{x})$ are the relative position and relative displacement of points $\mathbf{x}'$ and $\mathbf{x}$, respectively, and $\omega(|\boldsymbol{\xi}|)$ is the weight function. According to the classical continuum mechanics, the stress tensor can be expressed as

$$\boldsymbol{\sigma}^{pd} = \lambda\mathbf{tr}(\nabla\mathbf{u}^{pd})\mathbf{I} + \mathscr{G}\left[\nabla\mathbf{u}^{pd} + (\nabla\mathbf{u}^{pd})^T\right]. \tag{4}$$

with $\lambda$ representing Lame's material constant and $\mathscr{G}$ representing shear modulus. The matrix $\mathbf{G}$ in Eq. (2) is defined as

$$\mathbf{G} = \begin{bmatrix} (\lambda + \mathscr{G})d_1 + \mathscr{G}(d_1 + d_2 + d_3) & (\lambda + \mathscr{G})d_4 & (\lambda + \mathscr{G})d_5 \\ (\lambda + \mathscr{G})d_4 & (\lambda + \mathscr{G})d_2 + \mathscr{G}(d_1 + d_2 + d_3) & (\lambda + \mathscr{G})d_6 \\ (\lambda + \mathscr{G})d_5 & (\lambda + \mathscr{G})d_6 & (\lambda + \mathscr{G})d_3 + \mathscr{G}(d_1 + d_2 + d_3) \end{bmatrix}, \tag{5}$$

The vector $\mathbf{g} = [g_1 \quad g_2 \quad g_3]^T$ in Eq. (3) and $\mathbf{d} = [d_1 \quad d_2 \quad d_3 \quad d_4 \quad d_5 \quad d_6]^T$ in Eq. (5) are defined as

$$\begin{bmatrix} \mathbf{g} \\ \mathbf{d} \end{bmatrix} = \mathbf{A}^{-1}\hat{\boldsymbol{\xi}}, \tag{6}$$

where

$$\hat{\boldsymbol{\xi}} = [\xi_1 \quad \xi_2 \quad \xi_3 \quad \xi_1^2 \quad \xi_2^2 \quad \xi_3^2 \quad \xi_1\xi_2 \quad \xi_1\xi_3 \quad \xi_2\xi_3]^T, \tag{7}$$

$$\mathbf{A} = \begin{bmatrix} \mathbf{A}_{11} & \mathbf{A}_{12} \\ \mathbf{A}_{21} & \mathbf{A}_{22} \end{bmatrix}, \tag{8}$$

$$\mathbf{A}_{11} = \int_{H_x} \omega(|\boldsymbol{\xi}|) \begin{bmatrix} \xi_1^2 & \xi_1\xi_2 & \xi_1\xi_3 \\ \xi_1\xi_2 & \xi_2^2 & \xi_2\xi_3 \\ \xi_1\xi_3 & \xi_2\xi_3 & \xi_3^2 \end{bmatrix} dV_{x'}, \tag{9}$$

$$\mathbf{A}_{12} = \int_{H_x} \omega(|\boldsymbol{\xi}|) \begin{bmatrix} \frac{\xi_1^3}{2} & \frac{\xi_1\xi_2^2}{2} & \frac{\xi_1\xi_3^2}{2} & \xi_1^2\xi_2 & \xi_1^2\xi_3 & \xi_1\xi_2\xi_3 \\ \frac{\xi_1^2\xi_2}{2} & \frac{\xi_2^3}{2} & \frac{\xi_2\xi_3^2}{2} & \xi_1\xi_2^2 & \xi_1\xi_2\xi_3 & \xi_2^2\xi_3 \\ \frac{\xi_1^2\xi_3}{2} & \frac{\xi_2^2\xi_3}{2} & \frac{\xi_3^3}{2} & \xi_1\xi_2\xi_3 & \xi_1\xi_3^2 & \xi_2\xi_3^2 \end{bmatrix} dV_{x'}, \tag{10}$$

$$\mathbf{A}_{21} = \int_{H_x} \omega(|\boldsymbol{\xi}|) \begin{bmatrix} \xi_1^3 & \xi_1^2\xi_2 & \xi_1^2\xi_3 \\ \xi_1\xi_2^2 & \xi_2^3 & \xi_2^2\xi_3 \\ \xi_1\xi_3^2 & \xi_2\xi_3^2 & \xi_3^3 \\ \xi_1^2\xi_2 & \xi_1\xi_2^2 & \xi_1\xi_2\xi_3 \\ \xi_1^2\xi_3 & \xi_1\xi_2\xi_3 & \xi_1\xi_3^2 \\ \xi_1\xi_2\xi_3 & \xi_2^2\xi_3 & \xi_2\xi_3^2 \end{bmatrix} dV_{x'}, \tag{11}$$

$$\mathbf{A}_{22} = \int_{H_x} \omega(|\boldsymbol{\xi}|) \begin{bmatrix} \frac{\xi_1^4}{2} & \frac{\xi_1^2\xi_2^2}{2} & \frac{\xi_1^2\xi_3^2}{2} & \xi_1^3\xi_2 & \xi_1^3\xi_3 & \xi_1^2\xi_2\xi_3 \\ \frac{\xi_1^2\xi_2^2}{2} & \frac{\xi_2^4}{2} & \frac{\xi_2^2\xi_3^2}{2} & \xi_1\xi_2^3 & \xi_1\xi_2^2\xi_3 & \xi_2^3\xi_3 \\ \frac{\xi_1^2\xi_3^2}{2} & \frac{\xi_2^2\xi_3^2}{2} & \frac{\xi_3^4}{2} & \xi_1\xi_2\xi_3^2 & \xi_1\xi_3^3 & \xi_2\xi_3^3 \\ \frac{\xi_1^3\xi_2}{2} & \frac{\xi_1\xi_2^3}{2} & \frac{\xi_1\xi_2\xi_3^2}{2} & \xi_1^2\xi_2^2 & \xi_1^2\xi_2\xi_3 & \xi_1\xi_2^2\xi_3 \\ \frac{\xi_1^3\xi_3}{2} & \frac{\xi_1\xi_2^2\xi_3}{2} & \frac{\xi_1\xi_3^3}{2} & \xi_1^2\xi_2\xi_3 & \xi_1^2\xi_3^2 & \xi_1\xi_2\xi_3^2 \\ \frac{\xi_1^2\xi_2\xi_3}{2} & \frac{\xi_2^3\xi_3}{2} & \frac{\xi_2\xi_3^3}{2} & \xi_1\xi_2^2\xi_3 & \xi_1\xi_2\xi_3^2 & \xi_2^2\xi_3^2 \end{bmatrix} dV_{x'}. \tag{12}$$

Note that for the 2D case, the vector $\mathbf{g}$ and $\mathbf{d}$ are reduced to $\mathbf{g} = [g_1 \quad g_2]^T$ and $\mathbf{d} = [d_1 \quad d_2 \quad d_3]^T$, respectively, and all the components with $\xi_3$ in matrix $\mathbf{A}$ and vector $\hat{\boldsymbol{\xi}}$ will be deleted. For plane strain problems, the matrix $\mathbf{G}$ is reduced to

$$\mathbf{G} = \begin{bmatrix} (\lambda + \mathcal{G})d_1 + \mathcal{G}(d_1 + d_2) & (\lambda + \mathcal{G})d_3 \\ (\lambda + \mathcal{G})d_3 & (\lambda + \mathcal{G})d_2 + \mathcal{G}(d_1 + d_2) \end{bmatrix}, \tag{13}$$

and for plane stress problems,

$$\mathbf{G} = \begin{bmatrix} \frac{E}{2(1-\nu)}d_1 + \mathcal{G}(d_1 + d_2) & \frac{E}{2(1-\nu)}d_3 \\ \frac{E}{2(1-\nu)}d_3 & \frac{E}{2(1-\nu)}d_2 + \mathcal{G}(d_1 + d_2) \end{bmatrix}, \tag{14}$$

here $\nu$ is Poisson's ratio, $E$ is Young's modulus.

## 3. Coupled peridynamics least square minimization and finite element method

Compared to FEM, PD is computationally expensive. To increase computational efficiency, a new framework for coupling PD with FEM is proposed in this work to take advantage of these two methods. A numerical method base on PDLSM-FEM is then applied to model quasi-static crack propagation. For completeness and brevity in presentation, the formulation of coupled PDLSM-FEM is outlined succinctly in this section, with more lengthy details presented in Appendix A.
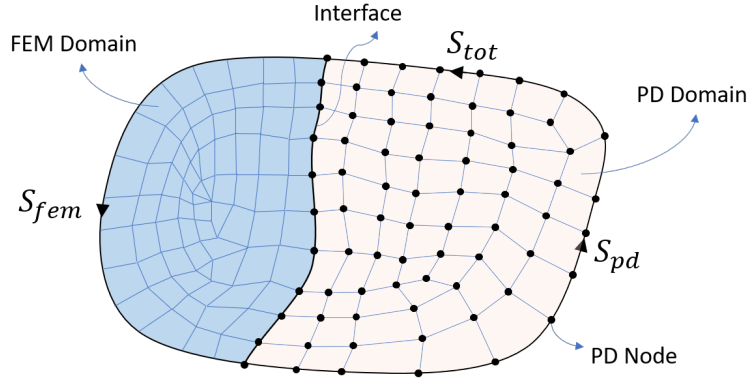


**Fig. 2:** A coupled PD-FEM model.

The coupled PDLSM-FEM is based on the weighted residual method (WRM) with the problem domain divided into a PD domain and a FEM domain, both of which are discretized into uniform or non-uniform elements, as illustrated in Fig. 2. To distinguish, the elements in the PD domain are called PD elements, and elements in the FEM domain are still called finite elements. Note that PD nodes on the interface of the PD domain and the FEM domain are also nodes of the finite element, and the interaction domains of these PD nodes are only determined from the PD domain, and the volumes of these PD nodes are calculated only from the PD elements. This method of coupling is straightforward and is easily introduced into commercial finite codes. The formulation of the coupling framework can be converted conveniently between pure PDLSM, pure FEM, and coupled PDLSM-FEM.

Applying the WRM on the equilibrium equations and the boundary conditions over the whole problem domain leads to

$$\int_{V_{tot}} \delta \mathbf{u}^T (\mathbf{L} + \mathbf{b} - \rho \ddot{\mathbf{u}}) dV - \int_{S_{tot}} \delta \mathbf{u}^T (\boldsymbol{\sigma} \mathbf{n} - \mathbf{T}) dS = 0, \tag{15}$$

where $\mathbf{T}$ is the external traction on the surface boundary, $\mathbf{n}$ is the unit normal vector of the boundary, $V_{tot}$ and $S_{tot}$ are the volume and surface of the whole domain respectively, and $\delta(\bullet)$ represents a virtual value. For the PD domain $V_{pd}$, the internal force vector takes on the integral form of Eq. (2), and for the FEM domain $V_{fem}$, it takes on the differential form of

$$\mathbf{L} = \nabla \cdot \boldsymbol{\sigma}. \tag{16}$$

For the surface of the PD domain, $S_{pd}$, the stress in the item $\delta \mathbf{u}^T \boldsymbol{\sigma} \mathbf{n}$ is derived based on the integral form of Eq. (3), and for the surface of the FEM domain, $S_{fem}$, $\delta \mathbf{u}^T \boldsymbol{\sigma} \mathbf{n}$ is canceled by applying Gauss theorem as

$$\int_{V_{fem}} \delta \mathbf{u}^T \mathbf{L} dV - \int_{S_{fem}} \delta \mathbf{u}^T \boldsymbol{\sigma} \mathbf{n} dS = - \int_{V_{fem}} \nabla \delta \mathbf{u} : \boldsymbol{\sigma} dV. \tag{17}$$

It is shown in the Appendix A that Eq. (15) can be transformed into the final governing equation for PDLSM-FEM as follows:

$$\mathbf{M} \ddot{\mathbf{u}}_g + \mathbf{K} \mathbf{u}_g = \mathbf{F}, \tag{18}$$

where $\mathbf{u}_g$, $\mathbf{M}$, $\mathbf{K}$ and $\mathbf{F}$ represent the global nodal displacement vector, the global equivalent nodal mass matrix, the global stiffness matrix, and the global equivalent nodal force, respectively. Details of the derivation are presented in Appendix A. For quasi-static crack propagation, the acceleration vector $\ddot{\mathbf{u}}_g$ is negligibly small, and Eq. (18) is reduced to

$$\mathbf{Ku}_g = \mathbf{F}, \tag{19}$$

which is the system equation to be solved implicitly in the current quasi-static crack propagation simulation. Comparing to explicit dynamic relaxation method, directly and implicitly solving Eq. (19) avoids a large number of iterations and is highly computationally efficient.

## 4. Quasi-static crack propagation simulation

In this section, we present an innovative quasi-static solution of crack growth problems based on the PDLSM-FEM technique and the linear elastic fracture mechanics (LEFM). The proposed method is an efficient way to simulate crack propagation when comparing to dynamic simulations. The crack propagation criterion is based on the maximum circumferential tensile stress evaluated from Stress Intensity Factors (SIFs), which are computed from the interaction integral ($I$-integral) of $J$-integral. As the $J$-integral is path independent, the proposed method is much more reliable and accurate than using near-tip stresses directly from the PD model which are sensitive to mesh refinement and are less accurate. In subsection 4.1, the $I$-integral proposed by Yau et al. (1980) to calculate SIFs is briefly reviewed. After that, we present the numerical integration of $I$-integral in subsection 4.2 and the failure criterion for quasi-static crack propagation in subsection 4.3. Finally, the simulation process is summarized in subsection 4.4

### 4.1. Stress intensity factors and interaction integral

In LEFM, the stress and displacement fields near the crack tip region can be evaluated by SIFs as follows. For mode $I$ loading,

$$\begin{cases} u_x = \frac{K_I(1+\nu)}{E}\sqrt{\frac{r}{2\pi}}\cos\frac{\theta}{2}\left(\kappa - 1 + 2\sin^2\frac{\theta}{2}\right), \\ u_y = \frac{K_I(1+\nu)}{E}\sqrt{\frac{r}{2\pi}}\sin\frac{\theta}{2}\left(\kappa + 1 - 2\cos^2\frac{\theta}{2}\right). \end{cases} \tag{20}$$

$$\begin{cases} \sigma_x = \frac{K_I}{\sqrt{2\pi r}}\cos\frac{\theta}{2}\left(1 - \sin\frac{\theta}{2}\sin\frac{3\theta}{2}\right), \\ \sigma_y = \frac{K_I}{\sqrt{2\pi r}}\cos\frac{\theta}{2}\left(1 + \sin\frac{\theta}{2}\sin\frac{3\theta}{2}\right), \\ \sigma_{xy} = \frac{K_I}{\sqrt{2\pi r}}\sin\frac{\theta}{2}\cos\frac{\theta}{2}\cos\frac{3\theta}{2} \end{cases} \tag{21}$$

For mode $II$ loading,

$$\begin{cases} u_x = \frac{K_{II}(1+\nu)}{E}\sqrt{\frac{r}{2\pi}}\sin\frac{\theta}{2}\left(\kappa + 1 + 2\cos^2\frac{\theta}{2}\right), \\ u_y = -\frac{K_{II}(1+\nu)}{E}\sqrt{\frac{r}{2\pi}}\cos\frac{\theta}{2}\left(\kappa - 1 - 2\sin^2\frac{\theta}{2}\right). \end{cases} \tag{22}$$

$$\begin{cases} \sigma_x = -\frac{K_{II}}{\sqrt{2\pi r}}\sin\frac{\theta}{2}\left(2 + \cos\frac{\theta}{2}\cos\frac{3\theta}{2}\right), \\ \sigma_y = \frac{K_{II}}{\sqrt{2\pi r}}\sin\frac{\theta}{2}\cos\frac{\theta}{2}\cos\frac{3\theta}{2}, \\ \sigma_{xy} = \frac{K_{II}}{\sqrt{2\pi r}}\cos\frac{\theta}{2}\left(1 - \sin\frac{\theta}{2}\sin\frac{3\theta}{2}\right) \end{cases} \tag{23}$$

in which $\nu$ is the Poisson ratio and the constant $\kappa$ is defined as $\kappa = (3 - \nu)/(1 + \nu)$ for plane stress and $\kappa = (3 - 4\nu)$ for plane strain problems. Since these field variables are expressed in terms of SIFs, accurate evaluation of the SIFs for

the analysis of fracture behavior is important. Different techniques have been proposed in the literature for evaluating SIFs. In this study, SIFs are computed based on the $J$-integral:

$$J = \int_{\Gamma} \left( w\mathcal{D}_{1j} - \sigma_{ij}\frac{\partial u_i}{\partial x_1} \right) n_j d\Gamma, \tag{24}$$

in which $w = \frac{1}{2}\sigma_{ij}\varepsilon_{ij}$ is the strain energy density, $n_j$ is the unit outward normal vector to the contour $\Gamma$ of integration, $\mathcal{D}$ is the Kronecker delta, and coordinates $(x_1, x_2)$ are taken to be the local crack tip coordinates with the $x_1$ axis parallel to the crack faces. For general 2D mixed-mode problems, the $J$-integral is related to SIFs as

$$J = \frac{K_I^2}{E^*} + \frac{K_{II}^2}{E^*}, \tag{25}$$

where $E^*$ is defined as

$$E^* = \begin{cases} E, & \text{plane stress,} \\ \frac{E}{1-v^2}, & \text{plane strain.} \end{cases} \tag{26}$$

in which $E$ is Young's modulus and $v$ is the Poisson ratio. To evaluate SIFs, we employ the $I$-integral based on $J$-integral which was first proposed by Yau et al. (1980). Consider two states of a cracked body, that is, the present state (1) called by $\left( u_i^{(1)}, \varepsilon_{ij}^{(1)}, \sigma_{ij}^{(1)} \right)$ and an auxiliary state (2) denoted by $\left( u_i^{(2)}, \varepsilon_{ij}^{(2)}, \sigma_{ij}^{(2)} \right)$, the $J$–integral for the sum of states (1) and (2) is:

$$J^{(1+2)} = \int_{\Gamma} \left( \frac{1}{2} \left( \sigma_{km}^{(1)} + \sigma_{km}^{(2)} \right) \left( \varepsilon_{km}^{(1)} + \varepsilon_{km}^{(2)} \right) \mathcal{D}_{1j} - \left( \sigma_{ij}^{(1)} + \sigma_{ij}^{(2)} \right) \frac{\partial}{\partial x_1} \left( u_i^{(1)} + u_i^{(2)} \right) \right) n_j d\Gamma. \tag{27}$$

Expanding and rearranging terms gives

$$J^{(1+2)} = J^{(1)} + J^{(2)} + I^{(1,2)}, \tag{28}$$

where $I^{(1,2)}$ is called the interaction integral ($I$-integral) for states (1) and (2), defined as

$$I^{(1,2)} = \int_{\Gamma} \left( w^{(1,2)}\mathcal{D}_{1j} - \sigma_{ij}^{(1)}\frac{\partial u_i^{(2)}}{\partial x_1} - \sigma_{ij}^{(2)}\frac{\partial u_i^{(1)}}{\partial x_1} \right) n_j d\Gamma, \tag{29}$$

where $w^{(1,2)}$ is the interaction strain energy defined by

$$w^{(1,2)} = \sigma_{ij}^{(1)}\varepsilon_{ij}^{(2)} = \sigma_{ij}^{(2)}\varepsilon_{ij}^{(1)}. \tag{30}$$

The $J$–integral definition in Eq. (25) can be written by the combined states (1) and (2) as

$$J^{(1+2)} = J^{(1)} + J^{(2)} + \frac{2}{E^*} \left( K_I^{(1)}K_I^{(2)} + K_{II}^{(1)}K_{II}^{(2)} \right), \tag{31}$$

Equating Eq. (28) and Eq. (31) leads to

$$I^{(1,2)} = \frac{2}{E^*} \left( K_I^{(1)}K_I^{(2)} + K_{II}^{(1)}K_{II}^{(2)} \right). \tag{32}$$

Making the choice of auxiliary state (2) as the pure mode $I$ asymptotic fields with $K_I^{(2)} = 1$ and $K_{II}^{(2)} = 0$ gives SIF of mode $I$ for state (1) in terms of the interaction integral

$$K_I^{(1)} = \frac{E^*}{2}I_{mode\ I}^{(1)}. \tag{33}$$

Similarly, making auxiliary state (2) as the pure mode $II$ asymptotic fields with $K_I^{(2)} = 0$ and $K_{II}^{(2)} = 1$ gives SIF of mode $II$ for state (1) as

$$K_{II}^{(1)} = \frac{E^*}{2}I_{mode\ II}^{(1)}. \tag{34}$$

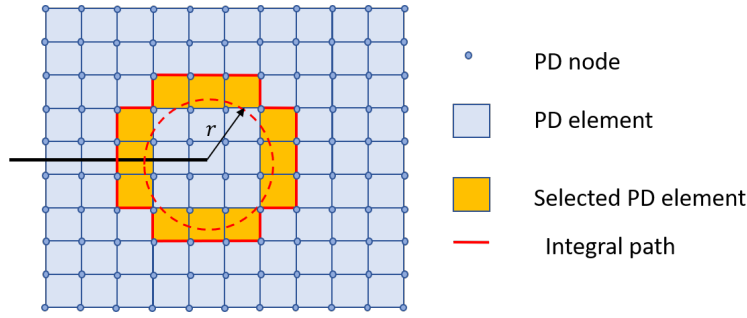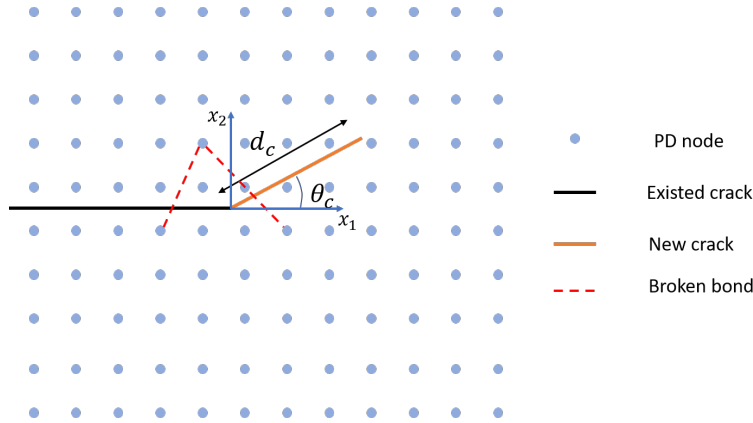**Fig. 3:** Contour of the $I$-integral.



**Fig. 4:** Schematic of crack growth.

## 4.2. Numerical Integration of $I$-Integral

SIFs are the most important parameters for the analysis of linear fracture behavior. To evaluate SIFs, we present an innovative method of numerical integration of $I$-integral over a path of PD nodes in this subsection.

To determine the $I$-integral contour, we propose the following guiding principle: (1) the integral contour should stay outside of and yet follow closely a base circle with desired size centered at the crack tip; (2) the selection of contour segments should allow easy and automatic implementation in the simulation; (3) the union of all contour segments must form a continuous path; and (4) no part of the contour goes inside the base circle.

To determine the contour, the PD domain is first discretized into 4-noded PD elements (quadrilateral elements), as illustrated in Fig. 3. A base circle with a specified radius $r$ is defined, shown by the red dot line in the figure. Next, PD elements forming the contour are selected based on this criterion: the selected elements must have either 2 or 3 nodes outside the base circle (yellow elements in the figure). Connecting consecutively all outside the base circle nodes of the selected elements forms the integral contour, as illustrated by the solid red lines in the figure. Although not shown herein, if the domain is discretized with 3-noded PD elements (triangle elements), we can treat these 3-noded elements as 4-noded elements with the fourth node and third node collapsed together. Note that, although we have the PD element concept here, the numerical implementation of PDLSM in the PD domain is a meshless method, rather than an element-based method. With the segments of the contour from each selected PD element, the value of interaction integral $I^{(1,2)}$ can be evaluated as

$$I^{(1,2)} = \sum_{e=1}^{N_{se}} \sum_{p=1}^{1 \text{ or } 2} \left( F_{(p)} + F_{(p+1)} \right) \frac{l_p}{2}, \tag{35}$$

where $l_p$ is the length of the segment between nodes $(p)$ and $(p+1)$, $N_{se}$ is the number of selected PD elements, and

$F_{(p)}$ denotes the integrand at node $(p)$ as:

$$F_{(p)} = \left( w^{(1,2)} \mathscr{D}_{1j} - \sigma_{ij}^{(1)} \frac{\partial u_i^{(2)}}{\partial x_1} - \sigma_{ij}^{(2)} \frac{\partial u_i^{(1)}}{\partial x_1} \right) n_j, \tag{36}$$

here the normal vector **n** can be determined by right-hand rule as:

$$\mathbf{n} = \begin{cases} \frac{x_{2(p)} - x_{2(p+1)}}{l_p} \mathbf{i} + \frac{x_{1(p+1)} - x_{1(p)}}{l_p} \mathbf{j}, & z > 0, \\ \frac{x_{2(p+1)} - x_{2(p)}}{l_p} \mathbf{i} + \frac{x_{1(p)} - x_{1(p+1)}}{l_p} \mathbf{j}, & z < 0. \end{cases} \tag{37}$$

in which $z$ is defined as below

$$z = \left( x_{1(p+1)} - x_{1(p)} \right) \left( x_{2(p+1)} - x_{2(t)} \right) - \left( x_{2(p+1)} - x_{2(p)} \right) \left( x_{1(p+1)} - x_{1(t)} \right), \tag{38}$$

where $x_{1(t)}$ and $x_{2(t)}$ are coordinates of the crack tip. The displacement, strain, and stress fields of state (1), that is, $u_i^{(1)}$, $\varepsilon_{ij}^{(1)}$, and $\sigma_{ij}^{(1)}$ are obtained by the PDLSM-FEM technique, while these field variables of the auxiliary state (2) are evaluated from LEFM formulas as in the Eqs. (20), (21), (22) and (23) with $K_I^{(2)} = 1$, $K_{II}^{(2)} = 0$ or $K_I^{(2)} = 0$, $K_{II}^{(2)} = 1$. With the displacement, strain, and stress fields of state (1) and of the auxiliary state (2), the value of $F_{(p)}$ at each node $(p)$ on the integral path is evaluated by Eq. (36), and then the $I$-integral $I^{(1,2)}$ is evaluated by Eq. (35). As described in section 4.1, assumed values of $K_I^{(2)} = 1$ and $K_{II}^{(2)} = 0$ lead to $I_{mode\ I}^{(1)} = I^{(1,2)}$, and assumed values of $K_I^{(2)} = 0$ and $K_{II}^{(2)} = 1$ lead to $I_{mode\ II}^{(1)} = I^{(1,2)}$. With the values of $I_{mode\ I}^{(1)}$ and $I_{mode\ II}^{(1)}$, SIFs are evaluated by Eq. (33) and Eq. (34). Note that a transformation from global coordinates to local coordinates is needed to evaluate the SIFs.

### 4.3. Crack propagation criterion

In crack propagation simulation, three propagation conditions need to be determined at each load step: (a) onset of propagation, i.e., whether or not the crack will propagate; (b) direction of propagation, i.e., along which direction the crack will propagate; and (c) amount of propagation, i.e., how long the crack will propagate. Criteria for conditions (a) and (b) are related to the underlying physics of crack propagation, while condition (c) is only an issue that needs to be dealt with in the numerical simulation.

For a general mixed-mode case, various criteria have been published by researchers to determine the first two conditions, such as the maximum energy release rate (Erdogan and Sih, 1963), the minimum strain energy density criteria (Sih, 1974), the maximum circumferential tensile stress (Erdogan and Sih, 1963). In this study, the maximum circumferential tensile stress theory is employed to determine the crack propagation direction. Based on this theory, the hoop stress reaches its maximum value on the plane of zero shear stress. For LEFM, the size of plastic zone at the crack tip is negligible and the singular term solutions of stresses at the crack tip are used to determine the crack propagation angle $\theta_c$, which is is defined as the angle between the line of crack and the crack growth direction (Fig. 4). The value of $\theta_c$ is determined by requiring the shear stress to become zero, and is found to be

$$\theta_c = \begin{cases} 2\tan^{-1}\left( \frac{K_I}{4K_{II}} - \frac{1}{4}\sqrt{\left(\frac{K_I}{K_{II}}\right)^2 + 8} \right) & \text{for } K_{II} > 0, \\ 2\tan^{-1}\left( \frac{K_I}{4K_{II}} + \frac{1}{4}\sqrt{\left(\frac{K_I}{K_{II}}\right)^2 + 8} \right) & \text{for } K_{II} < 0, \end{cases} \tag{39}$$

For a crack to propagate, the maximum circumferential tensile stress must reach a critical value. This results in an equivalent SIF in mixed-mode condition as

$$K_{eq} = K_I \cos^3 \frac{\theta_c}{2} - \frac{3}{2} K_{II} \cos \frac{\theta_c}{2} \sin \theta_c. \tag{40}$$

with $\theta_c$ determined by Eq. (39). If $K_{eq} > K_{Ic}$, in which $K_{Ic}$ is the fracture toughness, the crack will propagate in the direction of $\theta_c$, as shown in Fig. 4.

Most published criteria deal with only conditions (a) and (b), i.e., the onset of propagation and direction of propagation, and do not address condition (c), i.e., the amount of crack propagation. In the physical world, how much the crack will propagate depends on the body geometry and loading mechanism. If crack growth is unstable, once the propagation is triggered, $K_{eq}$ will remain larger than $K_{Ic}$, and the crack will propagate in an unstable manner until ultimate failure. If crack growth is stable, once the crack starts to propagate, $K_{eq}$ will drop below $K_{Ic}$, and crack growth will stop. Crack growth therefore is infinitesimal in stable growth, and a load increase is needed for further crack growth.

In numerical simulation, once the criterion for crack propagation is met, a somewhat arbitrary yet reasonable amount of crack growth must be assumed in each load step. The assumed crack growth amount is ultimately limited to the resolution of the numerical model. Since the fine PD elements near the crack tip represent the limit of the model resolution, we propose that the crack propagation amount should be comparable to the minimum characteristic length $\Delta_{min} = \sqrt{A_{min}}$ of PD nodes ($A_{min}$ represents minimum PD node's area), for example $\alpha$ times the $\Delta_{min}$, with $\alpha$ in the range of 0.5 to 1.5.

In the simulation, we implement the technique to model crack growth as following. We pre-define the amount of crack growth $d_c$ based on the PD elements size in each load step. Whenever the condition $K_{eq} > K_{Ic}$ is reached, the crack will propagate an amount $d_c$ along the direction of $\theta_c$. All bonds crossing the path of $d_c$ will be treated as broken with their bond status parameter $\mu$ updated from 1 to 0.

Depending on the value of $d_c$ and the level of load increment, it is possible that in stable crack propagation, after the crack propagates one $d_c$, several load increments are needed before $K_{eq}$ rises above $K_{Ic}$ again. On the other hand, in unstable crack propagation, once the propagation is triggered, $K_{eq}$ remains above $K_{Ic}$ no matter how much the crack propagates. In this case, the load level is kept unchanged, and the crack will continue to propagate in increment of $d_c$ in our simulation.

## 4.4. Step by step simulation process and flowchart

The simulation process is described step by step here to present a whole picture view of our model. A small load in terms of prescribed displacements is applied to the domain firstly, and the global stiffness $\mathbf{K}$ and global equivalent nodal force $\mathbf{F}$ are computed as described in Appendix A. Then the displacement field $\mathbf{U} = \mathbf{K}^{-1}\mathbf{F}$, and the field of strain and stress are solved. The strain and stress of the PD domain are obtained by Eq. (A.3) and Eq. (A.5), respectively. In the FEM domain, strain and stress are calculated by FEM formulas and for the PD-FEM interface, the nodal stresses and strains are calculated by the average of FEM and PD formulations. With the fields of displacement, strain, and stress, the SIFs, $K_I$ and $K_{II}$ are calculated according to Eqs. (33), (34), (35), and (36) for each crack tip. Next, the crack growth direction $\theta_c$ and equivalent SIF $K_{eq}$ are obtained by Eq. (39) and Eq. (40), respectively. If $K_{eq} > K_{Ic}$, the crack will grow along the direction $\theta_c$ by length $d_c$, with the new crack represented by a fictitious segment from the old crack tip to the new crack tip. All bonds passing through the new crack will be broken, so that the bond status parameter $\mu$ of these bonds will be updated, as well as the global stiffness $\mathbf{K}$, which becomes more compliant. If $K_{eq} < K_{Ic}$, the load will be increased by small increments until $K_{eq}$ exceeds $K_{Ic}$, and the simulation goes to the next iteration. Fig. 5 shows the flowchart of the quasi-static crack propagation simulation. In the simulation, $K_{eq}$ and $\theta_c$ for each crack tip are obtained and then the positions of new crack tips are determined, therefore this simulation method can handle multiple cracks.

## 5. Numerical results

To demonstrate the capability of the simulation model developed in this work, three plane stress examples are conducted and presented in this section. The first example is an infinite plate with an inclined crack at its center subjected to uniform far-field tension, in mixed-mode loading. The second and third examples are a disk-shaped plate and a diagonal plate with a pre-existing crack under displacement loading. In the first example, we investigate the SIFs of the infinite plate and compare the results against analytical solutions to demonstrate the accuracy of the proposed method, and a similar simulation by X-FEM can be found in (Khoei, 2015). In the second and third examples, we simulate the quasi-static crack growth of the two plates to show the capability of the proposed method to simulate crack propagation.

Note that the influence function $\omega(|\boldsymbol{\xi}|)$ may affect the accuracy in numerical implementation. In this paper, we
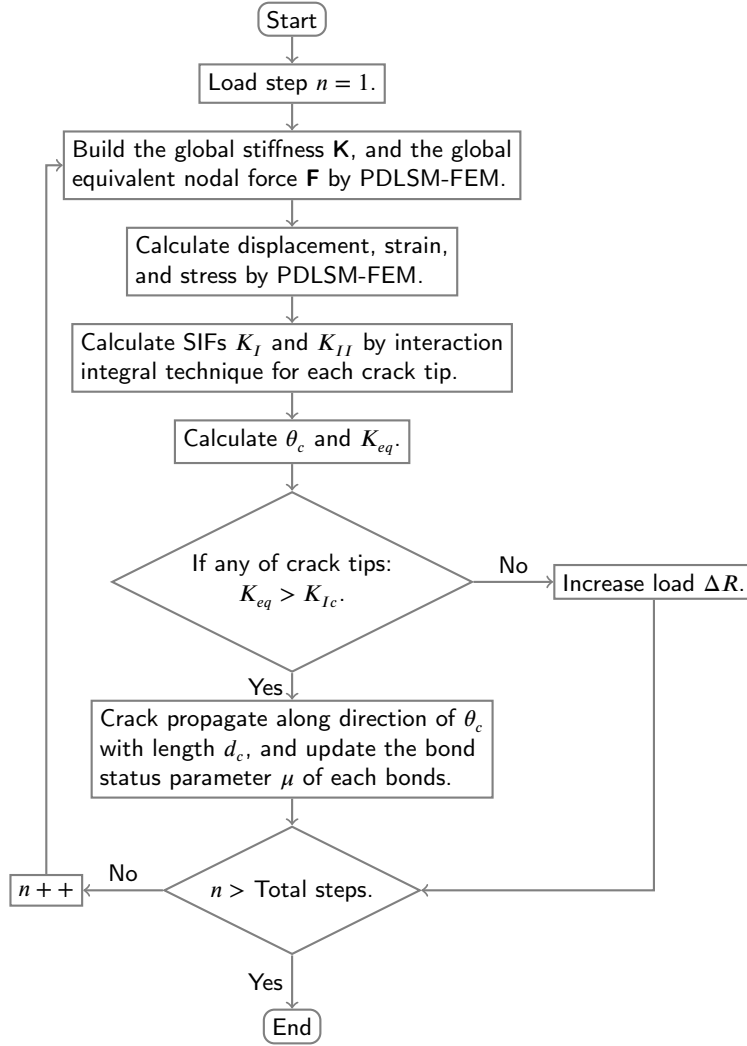
**Fig. 5:** Flowchart of crack propagation simulation.

specify the influence function as a Gaussian distribution in the form of

$$\omega(|\boldsymbol{\xi}|) = e^{-(\frac{|\boldsymbol{\xi}|}{a\delta_{(i)}})^2}, \tag{41}$$

here, $a$ is a constant and we define it as a *non-local factor*.

### 5.1. An infinite plate with an inclined crack for verifying SIFs

As shown in Fig. 6a, a square plate with a central inclined crack is under uniform tension $\sigma = 70$ Mpa. The material constants of the plate are specified as Young's modulus $E = 70$ GPa, Poisson's ratio $v = 0.33$. The edge length of the plate is $W = 1$ m, and the crack length is defined as $2a = 40$ mm. As the ratio $W/a = 50$ is sufficiently large, we can approximately treat this plate as an infinite plate. At the center of the plate, a small square sub-domain with size $l = 0.1$ m is defined as a PD domain, and the remaining part is defined as a FEM domain. The FEM domain is discretized as coarse 4-noded mesh, and the PD domain is discretized as very fine 4-noded PD elements (total of 1521) as shown in Fig. 6b, or discretized as very fine 3-noded PD elements (total of 3450) as shown in Fig. 6c. The
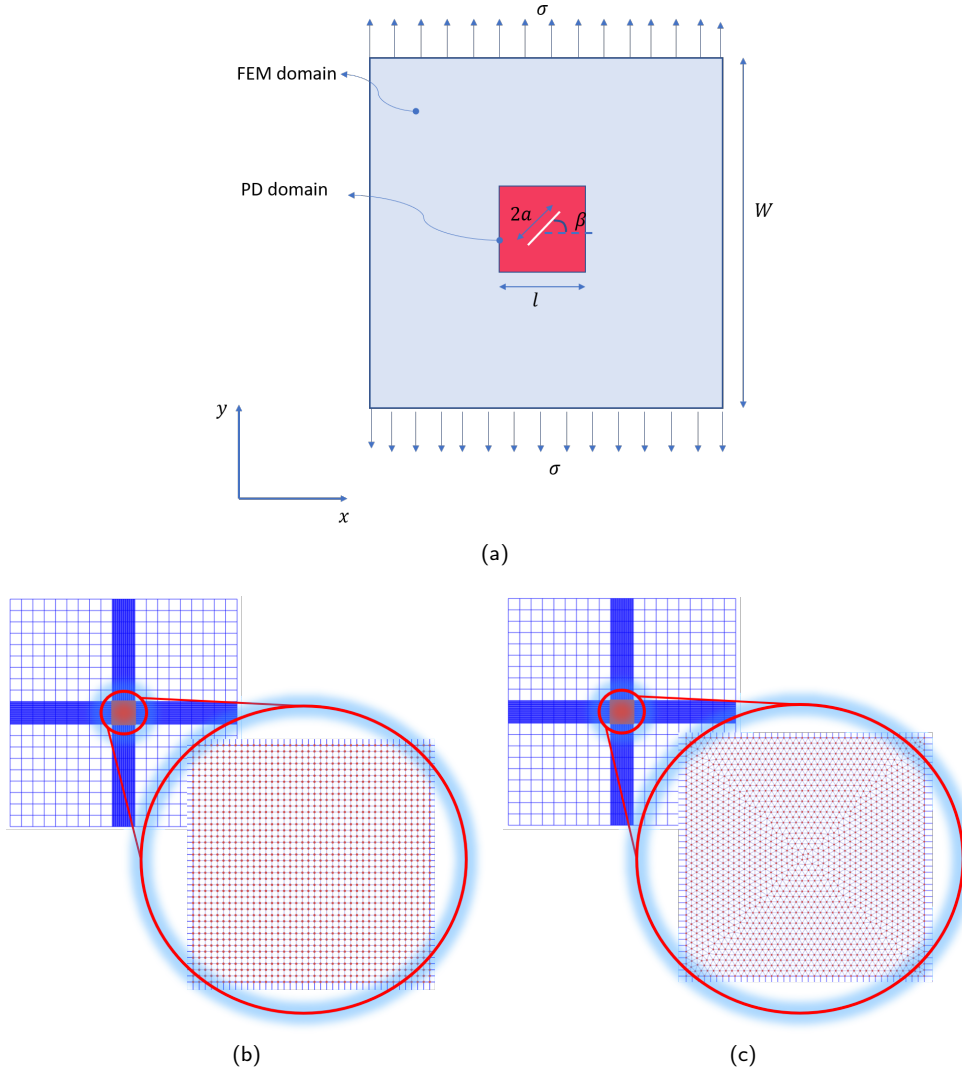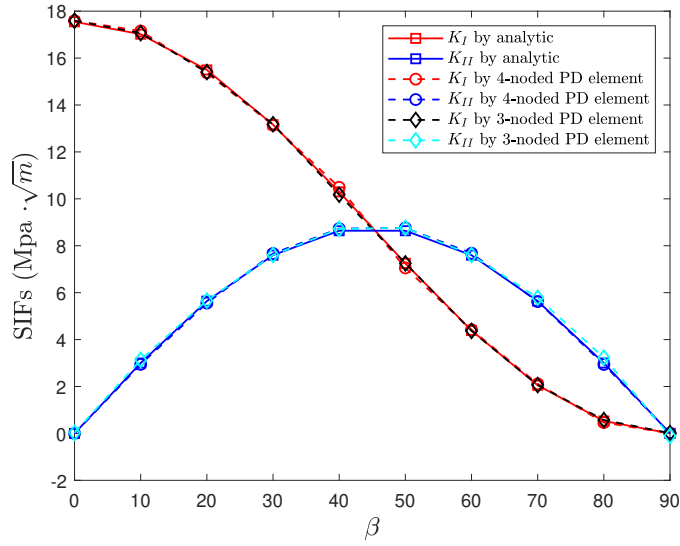
**Fig. 6:** Infinite plate with a central inclined crack: (a) Geometry, (b) 4-noded PD elements, (c) 3-noded PD elements.

analytical solution of this example with SIFs defined for modes $I$ and $II$ as (Broek, 2012)

$$\begin{cases} K_I = \sigma\sqrt{\pi a}\cos^2\beta, \\ K_{II} = \sigma\sqrt{\pi a}\cos\beta\sin\beta. \end{cases} \tag{42}$$

The PDLSM-FEM analysis is performed with non-local factor $\alpha = 1/3$ for 4-noded PD elements and $\alpha = 1/4$ for 3-noded PD elements. The radius of the based circle for the $I$-integral path is defined as $r = m_r\Delta_{(n)}$, where $m_r = 6$ and $\Delta_{(n)}$ is the characteristic length of the node which is nearest to the crack tip. The horizon size is specified as $\delta_{(i)} = 4\Delta_{(i)}$. Fig. 7 shows the evaluations of SIFs $K_I$ and $K_{II}$ at various crack angle $\beta$ for the numerical and theoretical solutions. Obviously, the relative error is almost negligible and a remarkable agreement can be seen between the theoretical values and numerical results by 4-noded and 3-noded PD models. Fig. 8 shows the stress results by PDLSM-FEM analysis with 4-noded PD elements for the infinite plate with an inclined $\beta = 30°$ crack. Finally, the effect of integration radius $r = m_r\Delta_{(n)}$ on evaluation SIF $K_I$ by 4-noded PD elements for pure mode $I$ ($\beta = 0$) is studied and the results are shown in Fig. 9. As it shows, for $m_r = 2$, the relative error is the largest with value $e = 2.24\%$ and for $m_r \geq 4$, the relative error is less than 1%.

**Fig. 7:** Comparison of SIFs between the numerical and analytical solutions at various crack angle $\beta$.
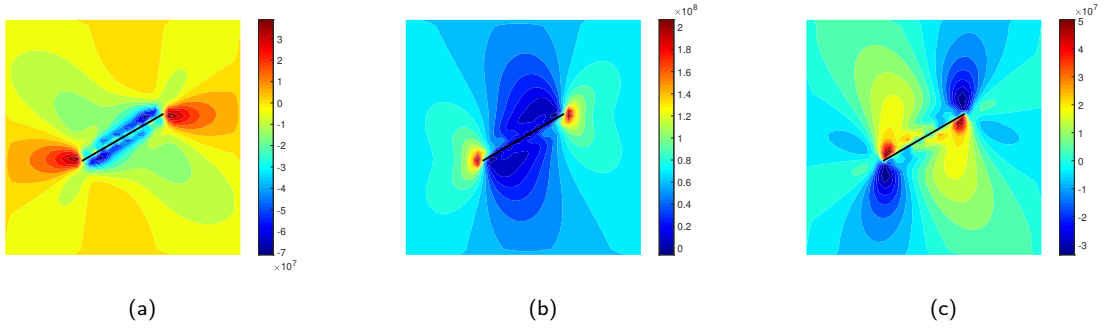


**Fig. 8:** Stress distributions for PD domain of the infinite plate with an inclined crack at angle $\beta = 30°$: (a) $\sigma_{xx}$, (b) $\sigma_{yy}$, (c) $\sigma_{xy}$.
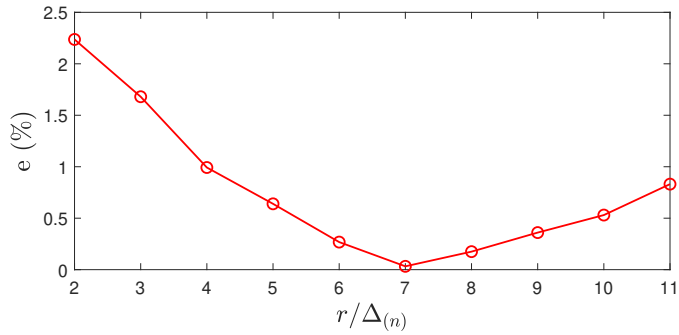


**Fig. 9:** Relative errors of SIF $K_I$ of model $I$ with various integration radius $r$.

## 5.2. A disk-shaped plate under displacement loading

This example is to simulate crack propagation of a disk-shaped plate. As shown in Fig. 10a, a disk-shaped plate with a pre-existing crack is under displacement loading with $u_1 = 0$ and $u_2$ increasing from zero with incremental $\Delta u_2 = 5.106 \times 10^{-6}$ m. The dimension of the plate is $W = 106.9$ mm, $a_0 = 44.3$ mm and thickness $B = 50$ mm. The material constants of the plate are Young's modulus $E = 33.5$ GPa, Poisson's ration $v = 0.3$, and fracture toughness $K_{Ic} = 1.09$ MPa$\sqrt{\text{m}}$. The whole plate is modeled by non-uniform discretization with a total of 5893 nodes and 5730 elements. The region of $-10.7$ mm $< y < 10.7$ mm is discretized with 1980 PD nodes and 1869 4-noded PD elements. The minimum characteristic length is $\Delta_{min} = 1.2$ mm and the crack growth length for each step is specified as $d_c = 1$ mm. The horizon size is $\delta_{(i)} = 4\Delta_{(i)}$, and the radius of the base circle for $I$-integral is $r = 6\Delta_{(n)}$. The non-local factor is $\alpha = 1/4$ in this example.

Fig. 11 shows the crack propagation and stress distributions of the disk-shaped plate at various load steps. As it shows, the crack propagates along the central horizontal line as expected and the stresses are concentrated at the crack tip. When the crack tip is far from the boundary of the domain (load step $n = 6$ and $n = 24$), the stress fields near the crack tip are similar to the analytical solutions.

Fig. 12a shows the SIF $K_I$ at various load steps. As it shows, the crack starts to propagate at load step $n = 6$ and after that, the SIF $K_I$ decreases. When $K_I < K_{Ic}$, the displacement loading increases with $\Delta u_2$. Fig. 12b shows the reaction force at various displacement loading. As it shows, the reaction force decreases overall after crack growth due to the increased structural compliance. Note that the increase of reaction force is due to an increase in displacement loading.
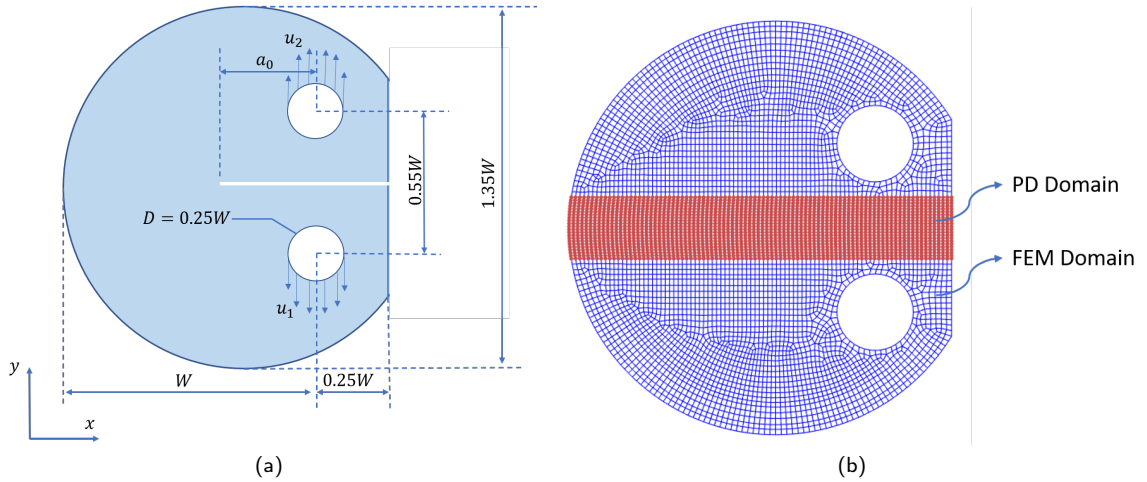


**Fig. 10:** A disk-shaped plate under displacement loading: (a) Geometry, (b) non-uniform mesh.

## 5.3. A diagonal plate under displacement loading

This example is to simulate crack propagation of a diagonal plate with a pre-existing inclined crack. As shown in Fig. 13a, a diagonal plate with size 150 mm × 150 mm × 5mm is under displacement loading with $u_1 = 0$ and $u_2$ increasing from zero with incremental $\Delta u_2 = 1.689 \times 10^{-4}$ m. The crack inclined angle is $\beta = 62.5°$ and its length is specified as $2a = 45$ mm. The radius of the loading hole is $r = 8$ mm and the distance between the center of the hole and the corner of the plate is specified as $b = 25$ mm. This plate is made of a brittle polymer called polymethylmethacrylate (PMMA) whose Young's modulus, Poisson ratio, and fracture toughness are $E = 2.94$ GPa, $v = 0.38$, and $K_{Ic} = 1.33$ MPa, respectively. As shown in Fig. 13b, the whole domain is discretized with a total of 5785 nodes and 5607 elements. The PD domain is discretized with uniform elements with size of 2 mm and it contains 3603 PD nodes and 3450 4-noded PD elements. The horizon size is specified as $\delta_{(i)} = 3\Delta_{(i)}$ and the radius of the base circle for the $I$-integral is $r = 6\Delta_{(n)}$. The non-local factor is $\alpha = 1/4$ in this example. The crack growth length for each step in this simulation is specified as $d_c = 1$ mm.
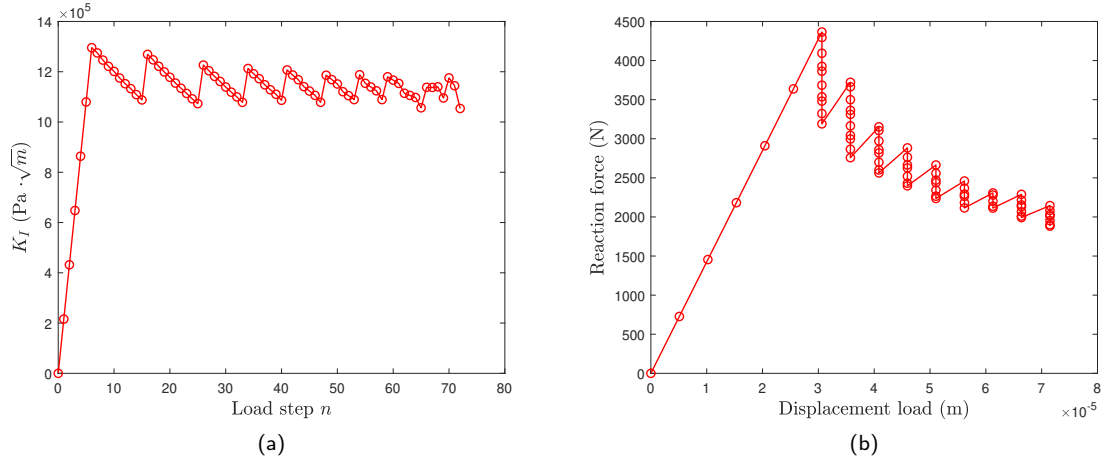
Fig. 14 shows the stress distributions of the diagonal plate at various load steps. As it shows, the stresses are concentrated at the crack tip. Fig. 15 shows the SIFs and the reaction force of the diagonal plate during crack propagation.
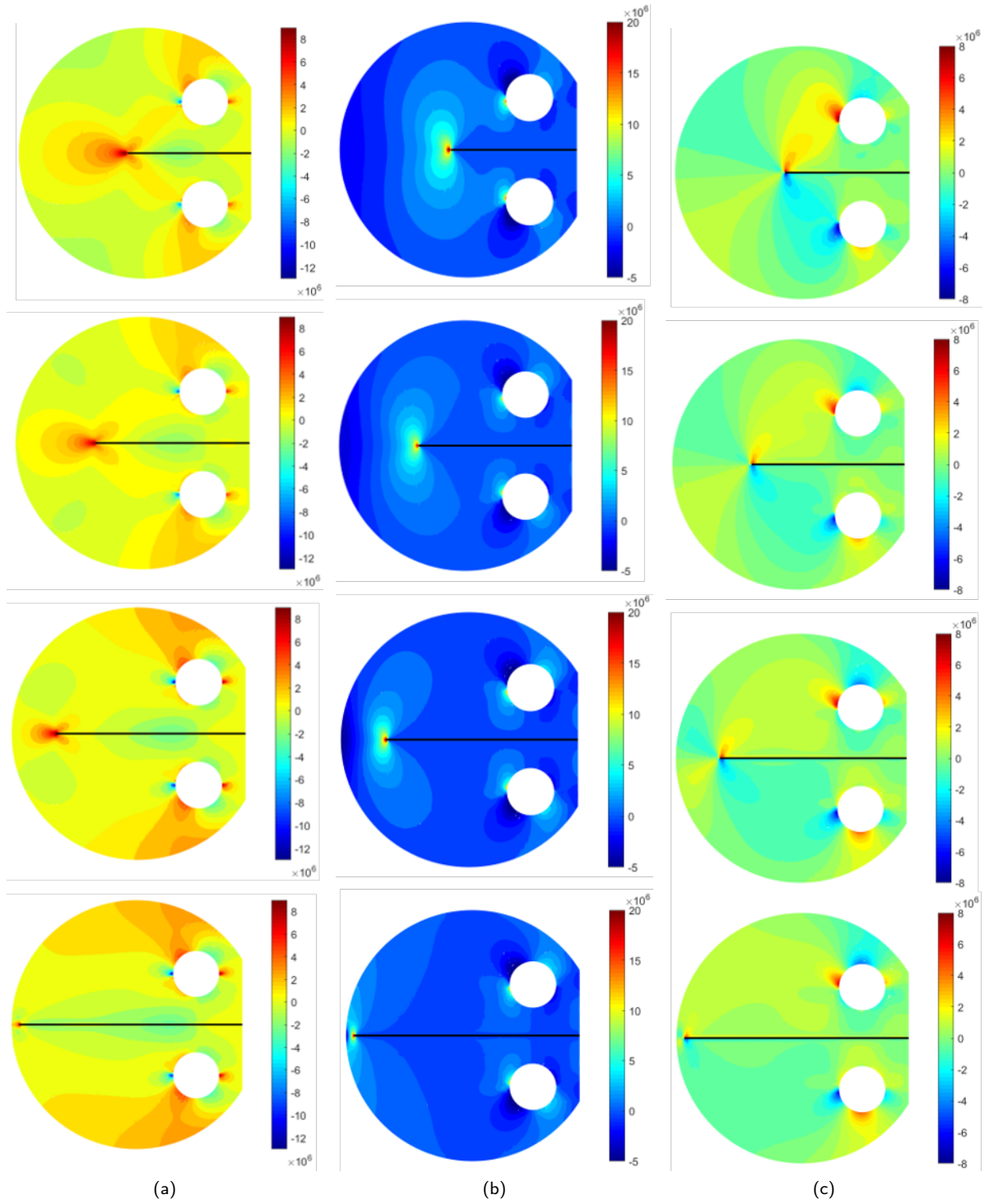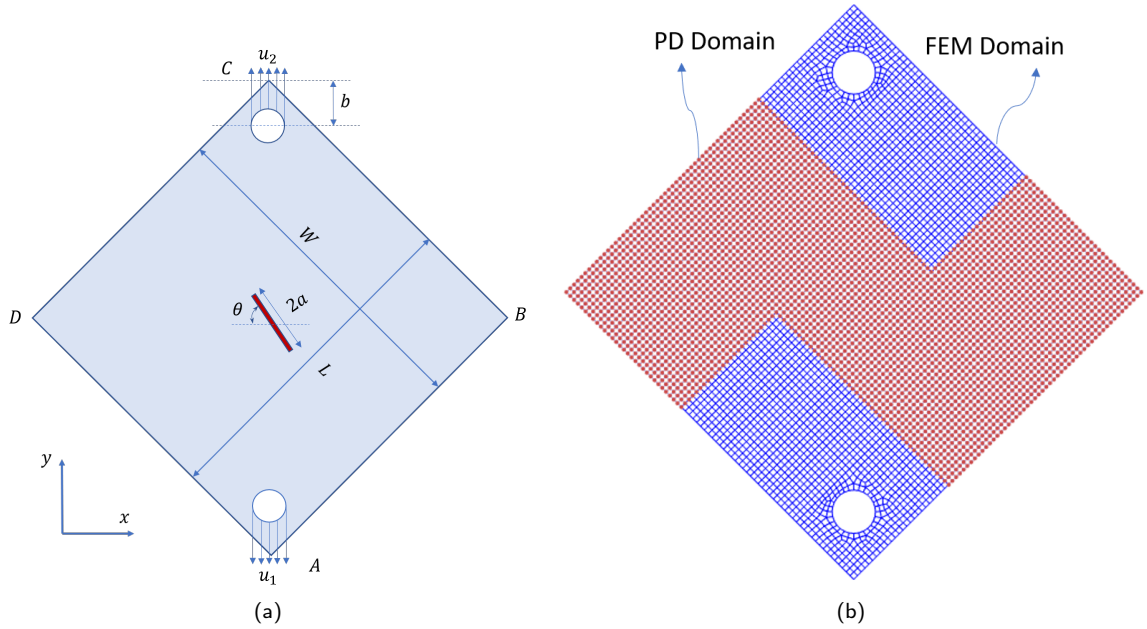
**Fig. 11:** Crack propagation and stress distributions of the disk-shaped plate at load step $n = 6$, $n = 24$, $n = 48$ and $n = 72$: (a) $\sigma_{xx}$, (b) $\sigma_{yy}$, (c) $\sigma_{xy}$.
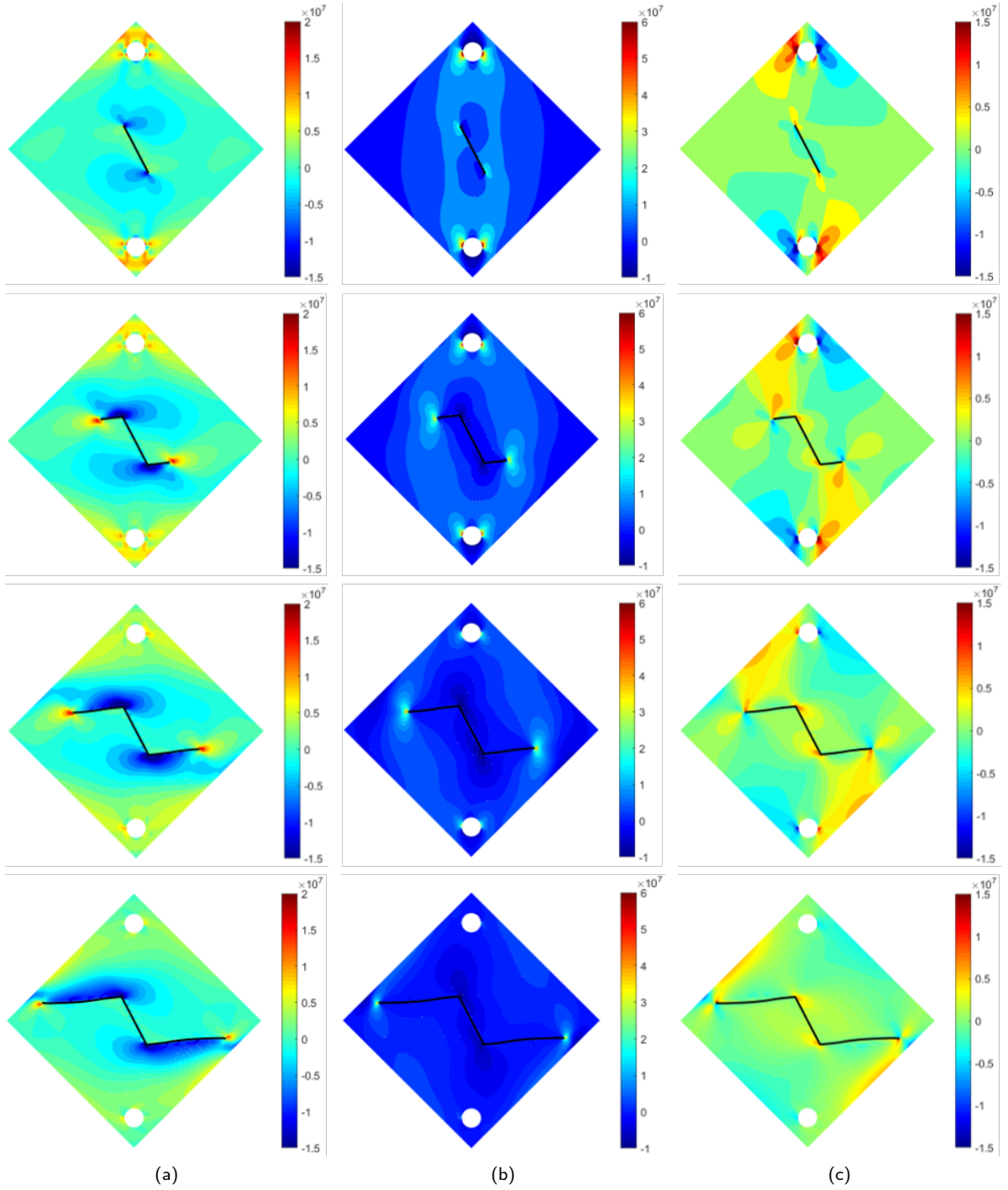
**Fig. 12:** The reaction force and SIF $K_I$ of the disk-shaped plate during crack growth: (a) SIF $K_I$ at various load steps $n$, (b) Reaction force at various displacement loading.

The crack of the plate starts to grow at load step $n = 5$, in which the equivalent SIF is $K_{eq} = 1.331$ Mpa $\approx K_{Ic}$, and the critical reaction force $P = 3362$ N, which is close to the experiment result $P_{cr} = 3192$ N (Ayatollahi and Aliha, 2009). Fig. 15b shows the reaction force decreases due to crack growth. As Fig. 15a shows, before the crack growth ($n < 5$), the plate is under pure mode $II$ loading as $K_I \approx 0$. After the crack growth but before the 30-th loading step, the plate is under mix-mode loading and the changing of the sign of $K_{II}$ makes the crack propagate with a zigzag shape. After the 30-th loading step, $K_{II} \approx 0$ and the plate is under pure mode $I$ loading. Fig. 16 shows the crack path of the diagonal plate which is in good agreement with the experimental observation.
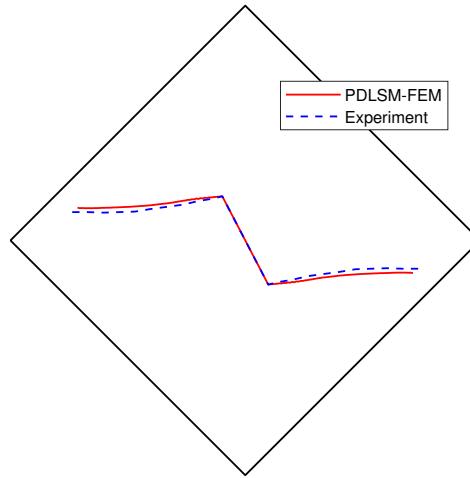


**Fig. 13:** A diagonal plate under displacement loading: (a) Geometry, (b) non-uniform mesh.

**Fig. 14:** Crack propagation and stress distributions of the diagonal plate at load step $n = 5$, $n = 24$, $n = 48$ and $n = 72$: (a) $\sigma_{xx}$, (b) $\sigma_{yy}$, (c) $\sigma_{xy}$.
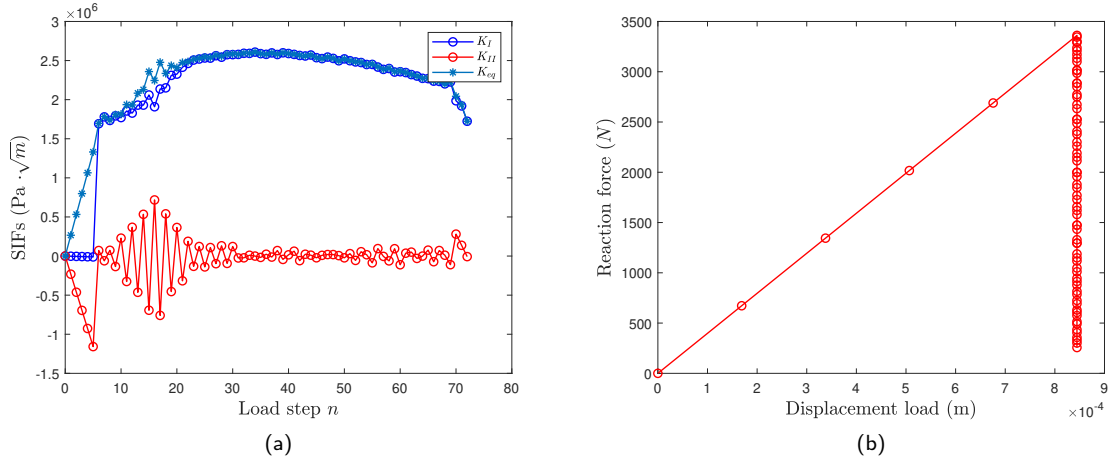
**Fig. 15:** The reaction force and SIFs of the diagonal plate during crack growth: (a) SIFs at various load steps $n$, (b) Reaction force at various displacement loading.



**Fig. 16:** Comparsion of crack growth path by PDLSM-FEM against experiment observation (Ayatollahi and Aliha, 2009).

## 6. Conclusions

In this paper, we develop a framework for coupling peridynamics least square minimization and finite element method (PDLSM-FEM) based on the weighted residual method, and a quasi-static crack propagation simulation method for mixed-mode loading. Compared with other PD methods, PDLSM does not require surface correction and volume correction. The PDLSM-FEM provides a unified way to couple PDLSM and FEM, and can be easily introduced into commercial finite element codes. The quasi-static crack propagation simulation method provides an efficient way to find the shape of the crack. The interaction integral of $J$-integral is applied to calculate the stress intensity factors (SIFs) in mixed mode loading. The criterion of the maximum circumferential tensile stress is utilized to predict the onset of crack propagation and direction of propagation. As the $J$-integral is path independent, the proposed method avoids using the near tip stresses from PDLSM-FEM which are sensitive to mesh refinement and therefore less accurate. New contributions in this work include the following: (1) developing a new framework for

coupling PDLSM and FEM; (2) pioneering a quasi-static method for simulating crack propagation in peridynamics; (3) developing an element-based approach for selecting the interaction integral contour; and (4) proposing and implementing an innovative method for handling peridynamic bond breakage and crack growth. One infinite plate with an inclined central crack under far-field tension is performed to calculate its displacement, stress, strain fields, and SIFs. The comparison of the SIFs between numerical and analytical solutions shows a good accuracy of the proposed method. Crack propagations in a disk-shaped plate and a diagonal plate under displacement loading are simulated, and the results show the capacity of the proposed method to model crack growth efficiently and satisfactorily.

## Appendix A   PDLSM-FEM

The formulas of coupled PDLSM-FEM are rather lengthy, therefore only the outline is presented in the main text. For completeness, detailed formulas are given here in this Appendix.

### A.1   Discretization of PD domain

The PDLSM model of a domain can be discretized with elements (named as PD element herein) by using commercial software, such as ANSYS due to its robust meshing ability. As illustrated in Fig. 17, a 2D PD domain is
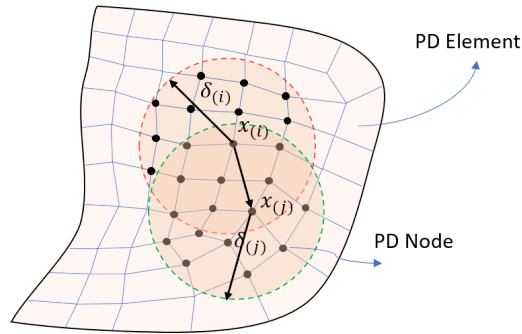


**Fig. 17:** PD domain discretization and interactions between node $\mathbf{x}_{(i)}$ and its family members.

discretized into PD elements and each PD element contains 4 PD nodes. Each PD element is divided into 4 parts with equal volume, and each part will count toward the volume of the associated node. Although not shown here, if the domain is discretized with 3-noded elements, a similar method will be used. It is worth noting that the PD node may not locate at the center of its volume, especially for these nodes locating on the boundary of the domain.

As shown in Fig. 17, the internal force vector at PD node $\mathbf{x}_{(i)}$ is calculated by including the interactions with its family members, $\mathbf{x}_{(j)}$, in the interaction domain. The interaction domain of node $\mathbf{x}_{(i)}$ depends on its horizon size $\delta_{(i)}$. The horizon size $\delta_{(i)}$ of node $\mathbf{x}_{(i)}$ is specified as $\delta_{(i)} = m\Delta_{(i)}$, with $m$ being an constant and the characteristic length $\Delta_{(i)} = \sqrt{A_{(i)}}$, which depends on the area $A_{(i)}$ occupied by PD node $\mathbf{x}_{(i)}$. For non-uniform discretization, the rule to determine family members of node $\mathbf{x}_{(i)}$ is suggested by Hu et al. (2018) as

$$H_{\mathbf{x}_{(i)}} = \left\{ \mathbf{x}_{(j)} \in H_{\mathbf{x}_{(i)}} : \left| \mathbf{x}_{(j)} - \mathbf{x}_{(i)} \right| \leq \delta_{(i)} \cup \left| \mathbf{x}_{(j)} - \mathbf{x}_{(i)} \right| \leq \delta_{(j)} \right\}, \tag{A.1}$$

which ensures that the bond between nodes $\mathbf{x}_{(i)}$ and $\mathbf{x}_{(j)}$ is a paired interaction for either interaction domain. For node $\mathbf{x}_{(i)}$, there are $N_{(i)}$ family members within its interaction domain and the displacement set of these nodes is

$$\mathbf{u}^{(i)} = \begin{bmatrix} u_{1(i)} & u_{2(i)} & u_{1(2)} & u_{2(2)} & \cdots & u_{1(m)} & u_{2(m)} & \cdots & u_{1(N_{(i)})} & u_{2(N_{(i)})} \end{bmatrix}^T, \tag{A.2}$$

here, the subscript $(m)$ represents the $m$-th family member node $\mathbf{x}_{(m)}$ within the interaction domain of node $\mathbf{x}_{(i)}$ and the first family member is itself, $\mathbf{x}_{(i)}$. From Eq. (3), we obtain the discrete form of strain vector at node $\mathbf{x}_{(i)}$ as

$$\{\varepsilon\}^{pd}_{(i)} = [\varepsilon_x \quad \varepsilon_y \quad \gamma_{xy}]^T = \mathbf{C}^{(i)}\mathbf{u}^{(i)}, \tag{A.3}$$

$$
\mathbf{C}^{(i)} = \begin{bmatrix} -\sum_{m=2}^{N_{(i)}} \mu_{(im)}\omega_{(im)}g_{1(im)}V_{(m)} & 0 & \mu_{(i2)}\omega_{(i2)}g_{1(i2)}V_{(2)} & 0 \\ 0 & -\sum_{m=2}^{N_{(i)}} \mu_{(im)}\omega_{(im)}g_{2(im)}V_{(m)} & 0 & \mu_{(i2)}\omega_{(i2)}g_{2(i2)}V_{(2)} \\ -\sum_{m=2}^{N_{(i)}} \mu_{(im)}\omega_{(im)}g_{2(im)}V_{(m)} & -\sum_{m=2}^{N_{(i)}} \mu_{(im)}\omega_{(im)}g_{1(im)}V_{(m)} & \mu_{(i2)}\omega_{(i2)}g_{2(i2)}V_{(2)} & \mu_{(i2)}\omega_{(i2)}g_{1(i2)}V_{(2)} \\ \cdots & \cdots & \mu_{(iN_{(i)})}\omega_{(iN_{(i)})}g_{1(iN_{(i)})}V_{(N_{(i)})} & 0 \\ \cdots & \cdots & 0 & \mu_{(iN_{(i)})}\omega_{(iN_{(i)})}g_{2(iN_{(i)})}V_{(N_{(i)})} \\ \cdots & \cdots & \mu_{(iN_{(i)})}\omega_{(iN_{(i)})}g_{2(iN_{(i)})}V_{(N_{(i)})} & \mu_{(iN_{(i)})}\omega_{(iN_{(i)})}g_{1(iN_{(i)})}V_{(N_{(i)})} \end{bmatrix}, \tag{A.4}
$$

where the subscript $(im)$ represents the bond between node $\mathbf{x}_{(i)}$ and its $m$-th family member. From Eq. (A.3), the discrete form of stress vector at node $\mathbf{x}_{(i)}$ is

$$
\{\sigma\}_{(i)}^{pd} = \mathbf{D}\mathbf{C}^{(i)}\mathbf{u}^{(i)}, \tag{A.5}
$$

here, $\mathbf{D}$ is material stiffness matrix of elasticity material. For plane stress problem,

$$
\mathbf{D} = \frac{E}{1-v^2} \begin{bmatrix} 1 & v & 0 \\ v & 1 & 0 \\ 0 & 0 & \frac{1-v}{2} \end{bmatrix}, \tag{A.6}
$$

and for plane strain problem,

$$
\mathbf{D} = \frac{E}{(1-2v)(1+v)} \begin{bmatrix} 1-v & v & 0 \\ v & 1-v & 0 \\ 0 & 0 & \frac{1-2v}{2} \end{bmatrix}. \tag{A.7}
$$

From Eq. (2), we obtain the discrete form of the internal force vector at node $\mathbf{x}_{(i)}$ as

$$
\mathbf{L}_{(i)}^{pd} = \mathbf{H}^{(i)}\mathbf{u}^{(i)}, \tag{A.8}
$$

$$
\mathbf{H}^{(i)} = \begin{bmatrix} -\sum_{m=2}^{N_{(i)}} \mu_{(im)}\omega_{(im)}\mathbf{G}_{(im)}V_{(m)} & \mu_{(i2)}\omega_{(i2)}\mathbf{G}_{(i2)}V_{(2)} & \cdots & \cdots & \mu_{(iN_{(i)})}\omega_{(iN_{(i)})}\mathbf{G}_{(iN_{(i)})}V_{(N_{(i)})} \end{bmatrix}. \tag{A.9}
$$

The bond status parameter $\mu_{(im)}$ in Eq. (A.4) and Eq. (A.9) is determined by the failure criteria.

## A.2 Discretization of PDLSM-FEM domain

To couple PDLSM with FEM, the whole problem domain is divided into a FEM domain and a PD domain, and both domains are discretized into elements, as shown in Fig. 2. To distinguish, elements in the PD domain are called PD elements and elements in the FEM domain are still called finite elements. Note that PD nodes on the PD-FEM interface are also nodes of the finite element, and the interaction domains of these PD nodes are only determined from the PD domain, and the volumes of these PD nodes are calculated only from the PD elements.

Consider a 2-D discrete domain that contains $N$ nodes, of which $N^{pd}$ are PD nodes. For the $i$-th PD node $\mathbf{x}_{(i)}$, its displacement vector is $\mathbf{u}_{(i)} = [u_{1(i)} \quad u_{2(i)}]^T$ and can be expressed as

$$
\mathbf{u}_{(i)} = \mathbf{M}_{(i)}\mathbf{u}_g, \tag{A.10}
$$

here, $\mathbf{u}_g$ is the displacement set of all nodes (global displacement vector) and $\mathbf{M}_{(i)}$ is the mapping matrix from $\mathbf{u}_g$ to $\mathbf{u}_{(i)}$, with size $2 \times 2N$. The displacement set of the family members of the PD node $\mathbf{x}_{(i)}$, $\mathbf{u}^{(i)}$, can be expressed by global displacement vector as

$$
\mathbf{u}^{(i)} = \mathbf{M}^{(i)}\mathbf{u}_g, \tag{A.11}
$$

here, $\mathbf{M}^{(i)}$ is the mapping matrix from $\mathbf{u}_g$ to $\mathbf{u}^{(i)}$, with size $2N_{(i)} \times 2N$, and it can be specified as follows: if the $k$-th component of $\mathbf{u}^{(i)}$ and the $j$-th component of $\mathbf{u}_g$ are same, $M_{kj}^{(i)} = 1$, otherwise $M_{kj}^{(i)} = 0$. The matrix $\mathbf{M}_{(i)}$ is determined in a similar way. Substituting Eq. (A.11) into Eq. (A.5) and Eq. (A.8), leads to the non-local stress vector and internal force vector expressed in terms of the global displacement vector as below,

$$\{\sigma\}_{(i)}^{pd} = \mathbf{DC}^{(i)}\mathbf{M}^{(i)}\mathbf{u}_g, \tag{A.12}$$

$$\mathbf{L}_{(i)}^{pd} = \mathbf{H}^{(i)}\mathbf{M}^{(i)}\mathbf{u}_g. \tag{A.13}$$

## A.3 Governing Equations of PDLSM-FEM

Applying the WRM to the equilibrium equations and the boundary conditions over the whole problem domain leads to the governing equation for PDLSM-FEM as expressed in Eq. (15) in the main text. Within the FEM domain, applying the Gauss theorem to Eq. (15) leads to

$$\int_{V_{fem}} \left[ \delta\mathbf{u}^T \rho\ddot{\mathbf{u}} + \delta(\{\epsilon\}^T)\{\sigma\} \right] dV + \int_{V_{pd}} \delta\mathbf{u}^T (\rho\ddot{\mathbf{u}} - \mathbf{L}^{pd}) dV + \int_{S_{pd}} \delta\mathbf{u}^T \sigma^{pd} \mathbf{n} dS = \int_{S_{tot}} \delta\mathbf{u}^T \mathbf{T} dS + \int_{V_{fem}} \delta\mathbf{u}^T \mathbf{b} dV + \int_{V_{pd}} \delta\mathbf{u}^T \mathbf{b} dV, \tag{A.14}$$

where $V_{fem}$ and $V_{pd}$ represent the volume of the FEM domain and PD domain respectively, and $S_{pd}$ represents the boundary of the PD domain. The virtual internal work by the internal force of the PD domain, $\delta U_B^{pd}$, can be expressed as

$$\delta U_B^{pd} = -\int_{V_{pd}} \delta\mathbf{u}^T \mathbf{L}^{pd} dV = \delta\mathbf{u}_g^T \mathbf{K}_b^{pd} \mathbf{u}_g, \tag{A.15}$$

where $\mathbf{K}_b^{pd} = -\sum_{i=1}^{N^{pd}} \mathbf{M}_{(i)}^T \mathbf{H}_{(i)} \mathbf{M}^{(i)} V_{(i)}$. Two adjacent PD nodes on the boundary of the PD domain, $S_{pd}$, define a PD boundary element (PDBE). As shown in Fig. 18, it is assumed that the displacement and traction force vary linearly between the two end nodes, $\mathbf{x}_{(\ell_1)}$ and $\mathbf{x}_{(\ell_2)}$, of the $\ell$-th PDBE as

$$\mathbf{u}_{(\ell)} = (1 - s)\mathbf{u}_{(\ell_1)} + s\mathbf{u}_{(\ell_2)}, \tag{A.16}$$

and

$$\mathbf{t}_{(\ell)}^{pd} = (1 - s)\mathbf{t}_{(\ell_1)}^{pd} + s\mathbf{t}_{(\ell_2)}^{pd}, \tag{A.17}$$

where $s$ is the local coordinate of the $\ell$-th PDBE with a unit normal vector $\mathbf{n}_{(\ell)}$ and length $\Gamma_{(\ell)}$. The traction force at the two end nodes of $\ell$-th PDBE can be expressed as
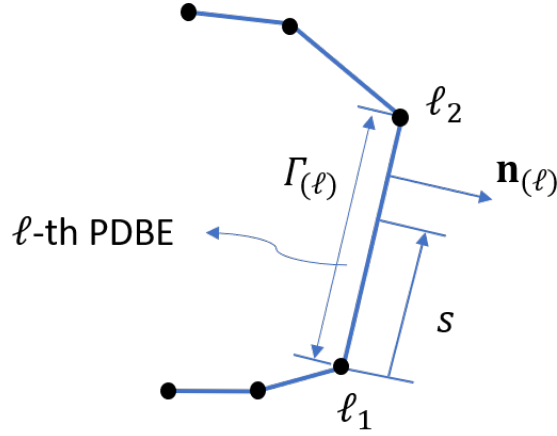
$$\mathbf{t}_{(\ell_i)}^{pd} = \sigma_{(\ell_i)}^{pd} \mathbf{n}_{(\ell)} = \mathbf{N}_{(\ell)} \{\sigma\}_{(\ell_i)}^{pd} \tag{A.18}$$

where $\mathbf{N}_{(\ell)}$ is defined as

$$\mathbf{N}_{(\ell)} = \begin{bmatrix} n_{1(\ell)} & 0 & n_{2(\ell)} \\ 0 & n_{2(\ell)} & n_{1(\ell)} \end{bmatrix}. \tag{A.19}$$

With this representation of $\mathbf{u}_{(\ell)}$ and $\mathbf{t}_{(\ell)}^{pd}$, the virtual internal work associated with PD domain boundary, $\delta U_S^{pd}$, can be evaluated as

$$\delta U_S^{pd} = \int_{S_{pd}} \delta\mathbf{u}^T \sigma^{pd} \mathbf{n} dS = \int_{S_{pd}} \delta\mathbf{u}^T \mathbf{t}^{pd} dS = \delta\mathbf{u}_g^T \mathbf{K}_s^{pd} \mathbf{u}_g, \tag{A.20}$$

**Fig. 18:** PD boundary elements.

where $\mathbf{K}_s^{pd}$ is defined as

$$\mathbf{K}_s^{pd} = \sum_{\ell=1}^{N_S^{pd}} \Gamma_{(\ell)} \left[ \left( \frac{1}{3}\mathbf{M}_{(\ell_1)} + \frac{1}{6}\mathbf{M}_{(\ell_2)} \right) \mathbf{N}_{(\ell)} \mathbf{DC}^{(\ell_1)}\mathbf{M}^{(\ell_1)} + \left( \frac{1}{6}\mathbf{M}_{(\ell_1)} + \frac{1}{3}\mathbf{M}_{(\ell_2)} \right) \mathbf{N}_{(\ell)} \mathbf{DC}^{(\ell_2)}\mathbf{M}^{(\ell_2)} \right], \tag{A.21}$$

in which $N_S^{pd}$ is the number of PDBE. The virtual work by the inertia force in the PD domain, $\delta U_I^{pd}$, can be evaluated as

$$\delta U_I^{pd} = \int_{V_{pd}} \delta \mathbf{u}^T \rho \ddot{\mathbf{u}} dV = \delta \mathbf{u}_g^T \mathbf{M}^{pd} \ddot{\mathbf{u}}_g, \tag{A.22}$$

where $\mathbf{M}^{pd} = \sum_{i=1}^{N^{pd}} \rho \mathbf{M}_{(i)}^T \mathbf{M}_{(i)} V_{(i)}$. Similarly, the virtual work by the external body force $\mathbf{b}$ in the PD domain, $\delta W_B^{pd}$, can be evaluated as

$$\delta W_B^{pd} = \int_{V_{pd}} \delta \mathbf{u}^T \mathbf{b} dV = \delta \mathbf{u}_g^T \mathbf{F}_b^{pd}, \tag{A.23}$$

where $\mathbf{F}_b^{pd} = \sum_{i=1}^{N^{pd}} \mathbf{M}_{(i)}^T \mathbf{b}_{(i)} V_{(i)}$. The virtual strain energy of the FEM domain, $\delta U^{fem}$, can be evaluated by FEM as

$$\delta U^{fem} = \int_{V_{fem}} \delta(\{\epsilon\}^T)\{\sigma\} dV = \delta \mathbf{u}_g^T \mathbf{K}^{fem} \mathbf{u}_g. \tag{A.24}$$

Similarly, the virtual work by the inertial force in the FEM domain, $\delta U_I^{fem}$, the virtual work by the external body force in the FEM domain, $\delta W_B^{fem}$, and the virtual work by the external traction force of the whole domain, $\delta W_S$, can be evaluated by FEM as follows:

$$\delta U_I^{fem} = \int_{V_{fem}} \delta \mathbf{u}^T \rho \ddot{\mathbf{u}} dV = \delta \mathbf{u}_g^T \mathbf{M}^{fem} \ddot{\mathbf{u}}_g, \tag{A.25}$$

$$\delta W_B^{fem} = \int_{V_{fem}} \delta \mathbf{u}^T \mathbf{b} dV = \delta \mathbf{u}_g^T \mathbf{F}_b^{fem}, \tag{A.26}$$

$$\delta W_S = \int_{S_{tot}} \delta \mathbf{u}^T \mathbf{T} dS = \delta \mathbf{u}_g^T \mathbf{F}_s. \tag{A.27}$$

As FEM is a mature technology, the details to obtain the $\mathbf{K}^{fem}$, $\mathbf{M}^{fem}$, $\mathbf{F}_b^{fem}$ and $\mathbf{F}_s$ are not shown here for conciseness. Substituting Eqs. (A.22), (A.23), (A.24), (A.25), (A.26) and (A.27) into Eq. (A.14) leads to the governing equation of this coupling model,

$$\mathbf{M}\ddot{\mathbf{u}}_g + \mathbf{K}\mathbf{u}_g = \mathbf{F}, \tag{A.28}$$

where the global equivalent nodal mass $\mathbf{M}$ is defined as

$$\mathbf{M} = \mathbf{M}^{pd} + \mathbf{M}^{fem}, \tag{A.29}$$

the global stiffness matrix $\mathbf{K}$ is defined as

$$\mathbf{K} = \mathbf{K}_b^{pd} + \mathbf{K}_s^{pd} + \mathbf{K}^{fem} \tag{A.30}$$

and the global equivalent nodal force $\mathbf{F}$ is defined as

$$\mathbf{F} = \mathbf{F}_b^{pd} + \mathbf{F}_b^{fem} + \mathbf{F}_s, \tag{A.31}$$

here, $\mathbf{M}$, $\mathbf{K}$ and $\mathbf{F}$ can be obtained by the assembling procedure as described previously. When $V_{pd} = 0$, Eq. (A.28) represents a pure traditional FEM model and when $V_{fem} = 0$, it represents a pure PD model. Thus, the formulation converts easily between PDLSM, FEM, and PDLSM-FEM.

# References

Ayatollahi, M., Aliha, M., 2009. Analysis of a new specimen for mixed mode fracture tests on brittle materials. Engineering Fracture Mechanics 76, 1563–1573. doi:10.1016/j.engfracmech.2009.02.016.

Bobaru, F., Foster, J.T., Geubelle, P.H., Silling, S.A., 2016. Handbook of peridynamic modeling. CRC press.

Broek, D., 2012. Elementary engineering fracture mechanics. Springer Science & Business Media.

Chu, B., Liu, Q., Liu, L., Lai, X., Mei, H., 2020. A rate-dependent peridynamic model for the dynamic behavior of ceramicmaterials. Computer Modeling in Engineering & Sciences 124, 151–178. doi:10.32604/cmes.2020.010115.

Erdogan, F., Sih, G., 1963. On the crack extension in plates under plane loading and transverse shear .

Foster, J., Silling, S.A., Chen, W., 2011. AN ENERGY BASED FAILURE CRITERION FOR USE WITH PERIDYNAMIC STATES. International Journal for Multiscale Computational Engineering 9, 675–688. doi:10.1615/IntJMultCompEng.2011002407.

Gerstle, W., Sau, N., Silling, S., 2005. PERIDYNAMIC MODELING OF PLAIN AND REINFORCED CONCRETE STRUCTURES , 16.

Hu, Y., Chen, H., Spencer, B.W., Madenci, E., 2018. Thermomechanical peridynamic analysis with irregular non-uniform domain discretization. Engineering Fracture Mechanics 197, 92–113. doi:10.1016/j.engfracmech.2018.02.006.

Jenabidehkordi, A., Rabczuk, T., 2019. The multi-horizon peridynamics. Computer Modeling in Engineering & Sciences 121, 493–500. doi:10.32604/cmes.2019.07942.

Jia, B., Ju, L., Wang, Q., 2019. Numerical simulation of dynamic interaction between ice and wide vertical structure based on peridynamics. Computer Modeling in Engineering & Sciences 121, 501–522. doi:10.32604/cmes.2019.06798.

Khoei, A.R., 2015. Extended finite element method theory and applications.

Kilic, B., Madenci, E., 2010a. An adaptive dynamic relaxation method for quasi-static simulations using the peridynamic theory. Theoretical and Applied Fracture Mechanics 53, 194–204. doi:10.1016/j.tafmec.2010.08.001.

Kilic, B., Madenci, E., 2010b. Coupling of peridynamic theory and the finite element method. Journal of Mechanics of Materials and Structures 5, 707–733. doi:10.2140/jomms.2010.5.707.

Le, Q.V., Bobaru, F., 2018. Surface corrections for peridynamic models in elasticity and fracture. Computational Mechanics 61, 499–518. doi:10.1007/s00466-017-1469-1.

Liu, Q., Xin, X., 2021. Revised non-ordinary state-based peridynamics and a new framework for coupling with finite element method. Engineering Fracture Mechanics 242, 107483. doi:10.1016/j.engfracmech.2020.107483.

Lubineau, G., Azdoud, Y., Han, F., Rey, C., Askari, A., 2012. A morphing strategy to couple non-local to local continuum mechanics. Journal of the Mechanics and Physics of Solids 60, 1088–1102. doi:10.1016/j.jmps.2012.02.009.

Madenci, E., Dorduncu, M., Barut, A., Phan, N., 2018. A state-based peridynamic analysis in a finite element framework. Engineering Fracture Mechanics 195, 104–128. doi:10.1016/j.engfracmech.2018.03.033.

Madenci, E., Dorduncu, M., Gu, X., 2019. Peridynamic least squares minimization. Computer Methods in Applied Mechanics and Engineering 348, 846–874. doi:10.1016/j.cma.2019.01.032.

Madenci, E., Oterkus, E., 2014. Peridynamic Theory and Its Applications. Springer New York, New York, NY. doi:`10.1007/978-1-4614-8465-3`.

Madenci, E., Oterkus, S., 2016. Ordinary state-based peridynamics for plastic deformation according to von Mises yield criteria with isotropic hardening. Journal of the Mechanics and Physics of Solids 86, 192–219. doi:`10.1016/j.jmps.2015.09.016`.

Ni, T., Zaccariotto, M., Zhu, Q.Z., Galvanetto, U., 2019. Static solution of crack propagation problems in Peridynamics. Computer Methods in Applied Mechanics and Engineering 346, 126–151. doi:`10.1016/j.cma.2018.11.028`.

Ren, H., Zhuang, X., Rabczuk, T., 2017. Dual-horizon peridynamics: A stable solution to varying horizons. Computer Methods in Applied Mechanics and Engineering 318, 762–782. doi:`10.1016/j.cma.2016.12.031`.

Seleson, P., 2014. Improved one-point quadrature algorithms for two-dimensional peridynamic models based on analytical calculations. Computer Methods in Applied Mechanics and Engineering 282, 184–217. doi:`10.1016/j.cma.2014.06.016`.

Sih, G.C., 1974. Strain-energy-density factor applied to mixed mode crack problems. International Journal of fracture 10, 305–321.

Silling, S., Askari, E., 2005. A meshfree method based on the peridynamic model of solid mechanics. Computers & Structures 83, 1526–1535. doi:`10.1016/j.compstruc.2004.11.026`.

Silling, S.A., 2000. Reformulation of elasticity theory for discontinuities and long-range forces. Journal of the Mechanics and Physics of Solids 48, 175–209.

Silling, S.A., Epton, M., Weckner, O., Xu, J., Askari, E., 2007. Peridynamic States and Constitutive Modeling. Journal of Elasticity 88, 151–184. doi:`10.1007/s10659-007-9125-1`.

Song, Y., Yan, J., Li, S., Kang, Z., 2019. Peridynamic modeling and simulation of ice craters by impact. Computer Modeling in Engineering & Sciences 121, 465–492. doi:`10.32604/cmes.2019.07190`.

Wang, Y., Han, F., Lubineau, G., 2019. A hybrid local/nonlocal continuum mechanics modeling and simulation of fracture in brittle materials. Computer Modeling in Engineering & Sciences 121, 399–423. doi:`10.32604/cmes.2019.07192`.

Warren, T.L., Silling, S.A., Askari, A., Weckner, O., Epton, M.A., Xu, J., 2009. A non-ordinary state-based peridynamic method to model solid material deformation and fracture. International Journal of Solids and Structures 46, 1186–1195. doi:`10.1016/j.ijsolstr.2008.10.029`.

Yau, J.F., Wang, S.S., Corten, H.T., 1980. A Mixed-Mode Crack Analysis of Isotropic Solids Using Conservation Laws of Elasticity. Journal of Applied Mechanics 47, 335–341. doi:`10.1115/1.3153665`.

Zaccariotto, M., Mudric, T., Tomasi, D., Shojaei, A., Galvanetto, U., 2018. Coupling of FEM meshes with Peridynamic grids. Computer Methods in Applied Mechanics and Engineering 330, 471–497. doi:`10.1016/j.cma.2017.11.011`.

Zaccariotto, M., Tomasi, D., Galvanetto, U., 2017. An enhanced coupling of PD grids to FE meshes. Mechanics Research Communications 84, 125–135. doi:`10.1016/j.mechrescom.2017.06.014`.

Zhang, H., Qiao, P., 2018. A state-based peridynamic model for quantitative fracture analysis. International Journal of Fracture 211, 217–235. doi:`10.1007/s10704-018-0285-8`.

Zhang, Y., Qiao, P., 2019. A new bond failure criterion for ordinary state-based peridynamic mode II fracture analysis. International Journal of Fracture 215, 105–128. doi:`10.1007/s10704-018-00341-x`.